NTNU – Trondheim
Norwegian University of
Science and Technology

Synthesis of Composite Nanoparticles with Magnetic Properties

Henrik Winther Solemslie

Chemical Engineering and Biotechnology
Submission date: June 2013
Supervisor: Wilhelm Robert Glomm, IKP
Co-supervisor: Gurvinder Singh, IKP

Norwegian University of Science and Technology
Department of Chemical Engineering

Abstract

There is a lot of research being done in inorganic nanoparticles for use in biomedicine as magnetic resonance imaging contrast-agents, where especially gadolinium is very interesting because of its 7 unpaired electrons. In this work a noval rout of synthesising cubic-shaped Fe_3O_4 nanoparticles, by using a sodium oleate batch from J. T. Baker, have been found. The synthesis rout differs from earlier reported methods by making a precursor of metal composite oleate before the thermal decomposition reaction. This general and novel route of synthesis have been used to synthesise cation-substituded $M_XFe_{3-X}O_4$ (M = Co, Gd) nanoparticles. Several compositions of cobalt iron oxide have been made with highly monodisperse cubic-shape and good size control, with particle size ranging from 4,46 nm to 13,29 nm. The same synthesis rout have been used to synthesis $Gd_XFe_{3-X}O_4$ particles with the compositions Fe:Gd = 1:0,1 and 1:0,5 where the different compositions gave spherical and cubic-shaped nanoparticles respectively, and the size range was between 1,2 nm and 7,4 nm. The synthesis rout has been proven to be able to synthesise Gd_2O_3, where the reaction time have been optimized to 4 hours. Samples of both the gadolinium iron oxide compositions and the pure gadolinium oxide have been phase-transferred to an aqueous media before their contrast-agent abilities were tested with MRI analysis. The MRI showed the samples increases the signal in the surrounding protons in both T1-weighted and T2-weighted images showing potential for further use of this synthesis rout in the production of MRI contrast-agent.

Sammendrag

Det har vært mye forskning innen uorganiske nanopartikler for bruk i biomedisin som MRI kontrast-midler, hvor spesielt gadolinium er veldig interessant grunnet dets 7 uparete elektroner. I dette arbeid har en ny måte å syntetisere kubisk formede Fe_3O_4 nanopartikler blitt funnet, ved bruke natrium oleate fra J.T. Baker. Syntese metoden er skiller seg fra tidligere rapporterte metoder ved at den starter med å lage en forløper av kompositt metal oleate før den termiske dekomponeringen. Denne generelle og nye syntesemetoden er brukt til å syntetisere kation-substituerte $M_XFe_{3-X}O_4$ (M = Co, Gd) nanopartikler. Flere komposisjoner av kobolt jern oksid har blitt laget med høy monodispersitet, kubiske fasong og god størrelses kontroll, med partikkelstørrelse mellom 4,46 nm og 13,29 nm. Den samme syntesemetoden har blitt brukt til å syntetisere $Gd_XFe_{3-X}O_4$ nanopartikler med komposisjonene Fe:Gd = 1:0,1 og 1:0,5, hvor de forskjellige komposisjonene hadde henholdsvis sfærisk, og kubisk form, og størrelsesorden mellom 1,2 nm og 7,4 nm. Syntesemetoden har vist seg å være i stand til syntetisere Gd_2O_3 nanopartikler, hvor reaksjonstiden har blitt optimalisert til 4 timer. Prøver med de forskjellige komposisjonene av jern gadolinium oksid og ren gadolinium oksid ble faseoverført til vannfase før deres egenskaper som kontrast-middel ble testet med MRI. MRI testen viste at prøvene øker signalstyrken til de omkringliggende protonene i både T1-vektlagt og T2-vektlagte bilder. Dette viser potensiale for syntesemetoden for videre å lage MRI kontrast-midler.

Preface

This master thesis was written at the Department of Chemical Engineering at the Norwegian University of Science and Technology during the spring of 2013. This master thesis was done under the subject TKJ4900.

I would first like to thank my main supervisor, Wilhelm Glomm and my co-supervisor Gurvinder Singh. Especially Gurvinder have been an enormous help with the practical and the writing of the thesis. I would also like to thank Axel Karl Gottfrid Nyman who helped me with the MRI analyses.

I would like to thank Høiskolens Chemikerforening who filled my whole life, the first couple of years in Trondheim, with friends and fun and which will always mean a great deal to me. I will also thank Trondhjems Studentersangforening, Pirum and the population of Sanger'n for, in my later years, overfilling my life with the expression: Syng, drikk og vær glad!

Finally, I would like to thank my girlfriend, who have been more than understanding and patient when I have been unreachable the last couple of weeks of my master work.

Henrik Winther Solemslie

Table of content

Abbreviations

Abbreviation	Unite
BE	Binding Energy
EDX	Energy-dispersive X-ray spectroscopy
FC	Field Cooled
FTIR	Fourier transformed infrared spectrometry
ICP-MS	Inductively coupled plasma mass spectrometry
KE	Kinetic energy
MRI	Magnetic resonance imaging
RF	Radio frequency
TEM	Transmission electron microscopy
XRD	X-ray diffraction
XPS	X-ray photoelectron spectroscopy
ZFZ	Zero field, zero cooled

List of figures

1. Introduction

Today, cancer is one of the most known and feared diseases which kills approximately 7,6 million people each year, i.e., 13 % of all deaths world wide alone [1]. Despite rapid technological progress in the diseases diagnostic in a last decade, the survival rate from cancer is still very low. Therefore, novel strategies should be developed for the accurate detection of early-stage cancer and subsequently, targeted therapy for its treatment. Recent advances in the nanomaterial synthesis have overcome difficulties associated with conventional detection techniques and target drug delivery. Materials in the nano range are not a new invention. They have existed in the world since the dawn of time, and the first to explore this field of science did it in the colloid and catalysts in the 70's and 80's. But the main reason for the big interest in the field not starting before decades later is that we did not have the imaging technology to investigate the materials [2]. Presently, wet chemical approaches have especially been recognized for their capability to produce a variety of metal oxide, and semiconductor nanoparticles with highly controlled size, shape, and composition by careful regulation of thermodynamic parameters and growth kinetics in liquid media under the assistance of selected solvents, ligands, surfactants and catalyst additives. Such nanoparticles find potential applications in catalysis [3-5], solar cell [6], electronic devices [7], storage devices [5, 8], sensors, and biomedical field [9-18]. Among them, magnetic nanoparticles, for example, iron oxide, have been widely used as a contrast agent in Magnetic Resonance Imaging (MRI) for the detection of cancer cells, and therapeutics.

However, MRI technique still faces difficulties in identifying cancer cells from the surrounding healthy cells. One of the tool used to help differentiate the MRI-signals are contrast-agents that affects the surroundings by either enhancing or reducing their MRI-signals. Iron oxide nanoparticles are super-paramagnetic in nature and possess low magnetic moment at room temperature which results in a low contrast in MRI. However, other types of magnetic nanoparticles possessing high magnetic moment, such as Co, Mn, Ni etc., can also be used to enhance the MRI contrast, but they are toxic, and less biocompatible. A possible solution to enhance MRI contrast is to use alloy oxide while retaining the biocompatibility. Furthermore it is very hard to stabilise the particles that enhance the signal for clinical use, most contrast-agents today are of the reducing type which are of inferior usefulness.

In this thesis work we have proposed a general and novel route for the synthesis of the cation-substituted $M_xF_{3-x}O_4$ (M = Co, Gd etc)[19-22] nanoparticles with controlled composition and rare earth metal oxide nanoparticles. These nanoparticles have been analysed with Transmission electron microscopy (TEM), Energy-dispersive X-ray spectroscopy (EDX), X-ray photoelectron spectroscopy (XPS), Zeta potential and Magnetic resonance imaging (MRI).

2. Theory

2.1 Synthesis of Iron oxide composite particles

Over the last decade, several different protocols have been developed for the synthesis of magnetic nanoparticles from physical methods such as biomineralization processes [23] and mechanical grinding to chemical methods as micro-emulsion methods [24], coprecipitation methods [25], sol-gel synthesis [26], electrochemical methods [27], sonochemical reaction [28], polyol methods [29], flame-assisted method [30], etc.

The chemical methods have especially been recognized for their capability to produce a variety of magnetic nanoparticles with better control over sizes, size distribution, crystalinity and phase purity. Thermal decomposition method is one of the most successful approaches which uses organometallic precursors such as metal-oleate and long chain fatty acids as a surfactant. The ratio of organometallic precursor to surfactant, solvent type, reaction temperature and time is crucial for controlling both the size and morphology if the nanoparticle [31]. There are two main methods within thermal decomposition, termed as heat-up and hot-injection. For the heat-up method, the reaction mixture is heated up slowly until nucleation occurs. For the hot-injection method, the organometallic precursor is injected in the boiling solvent [32]. The reactants decompose at high temperatures and become highly reactive "monomers". These monomers are responsible for inducing nucleation of the nanoparticle, and sustaining their subsequent enlargement/growth by Ostwald ripening process [33].

It has been investigated that the shape of the nanoparticles can be tuned by choosing the appropriate surfactant type. Use of oleic acid is known to produce spherical particles, while using deprotonated oleic acid, and therefore controlling its affinity to the surface, have given cubic-shaped particles. Another method is to introduce sodium oleate to the reaction. The growth of the particles is controlled by the surface energy of the growing facets. The production of spherical particles are caused by the surfactant being able to keep the surface energy equal around the particle, and therefore let the particle grow equally in all direction and thus become spherical. The cubic-shaped production is possible by controlling the amount of "free" surfactant available to bind to the growing facets [34]. The different facets ({100}, {110}, {111}) as shown in Figure 1 have different surface energy [35], where {100} is lowest and {111} is highest. The surfactants will first stabilize the high-energy facets, and thus induce growing on these first and resulting in cubic-shaped particles [36, 37].

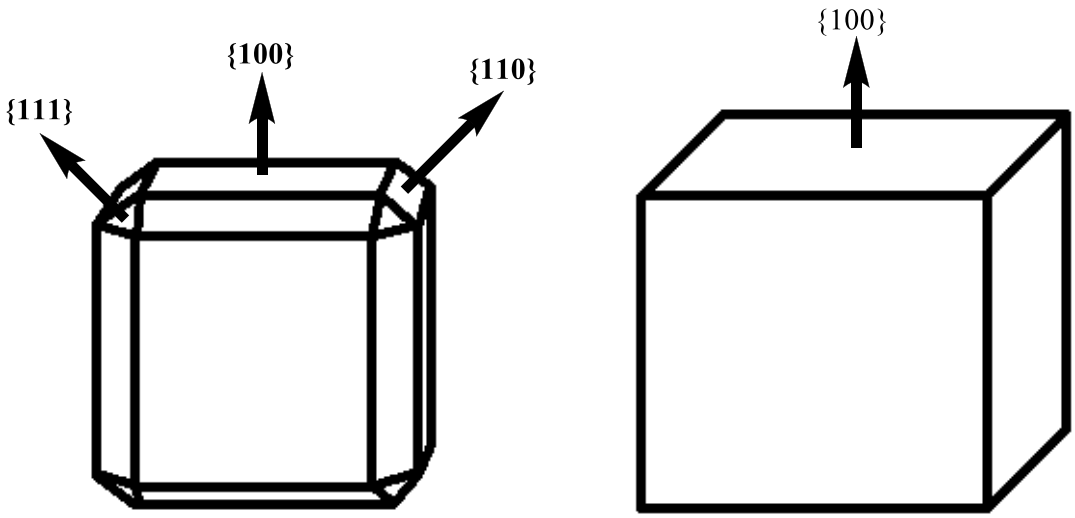

Figure 1: Growth process of cubic-shaped particles, with facets.

Even though iron oxide has been used earlier for liver imaging, they are not commonly used now. The iron oxide affected the magnetic resonance imaging by reducing the signal from the surroundings. This is inferior to MRI-enhancing contrast-agents since it is hard to differentiate between the contrast-agent reduced signal, and areas with lower signal, while the enhanced signals will differentiate it self from the rest of the image[38].

For composite particles, such as $CoFe_2O_4$ and $MnFe_2O_4$, Bao et al. have reported that the geometry may be controlled by the temperature. While using a heat-up method lowering the heating rate resulted in cubic-shaped particles. And with time at the reaction temperature these cubic-shaped particles grew more spherical [39, 40]. This is coherent with the facet-surface energy theory. A synthesis rout found by Mohapatra et al. uses ethanolamine as stabilizer, which also functionalized the surface of the particles to become highly hydrophilic [41]. This is very useful since particles from other synthesis methods needs to be extra coated with a hydrophilic layer.

2.2 Magnetism and basic magnetic resonance

The magnetic properties of materials can be explained by understanding the atomic structure. Each atom consists of three fundamentals parts. At the core of the nucleus, it consists of protons, which have a positive charge, and neutrons with no charge surrounded by negatively charged electrons, residing at different energy levels. How the atom reacts with others are dependent on the amounts of these particles. The primary way to differentiate the atoms is by the atomic number, which is the number of protons in the core. The atomic weight is the sum of numbers of protons and numbers of neutrons in the atom. Particles with the same atomic number, but different atomic weight are called isotopes. In a neutral atom there are equal number of protons and atoms, if there are more electrons it is called an anion with negative charge, and vice versa it is called a cation with a positive charge if there are more protons. The electrons around the core belong to different orbitals, which fills up in order as shown in Table 1 [42].

Table 1: Electron in different orbitals for different elements.

Atomic number	Element	1S	2s	2p	3s	3p	3d	4s	4p	4d	4f
1	H	1									
6	C	2	2	2							
17	Cl	2	2	6	2	5					
26	Fe	2	2	6	2	6	6	2			

A third property of the nucleus is spin. There are three types of motions present in an atom, electrons spinning around their own axis, electron orbiting the nucleus and the nucleus spinning round its own axis later referred to as spin or spin angular momentum. The spin, I, is found with a limited number of values in nature, zero, integral and half integral, and is determined by the atomic number and weight of the nucleus. Nuclei with even atomic number and even atomic weight has no spin (I=0). Such nuclei do not interact with external magnetic fields. Nuclei with even atomic weight and odd atomic number has an integral value for I (e.g.. 1, 2, 3) and nuclei with odd atomic weight has half-integral value of I(e.g.. ½, 3/2, 5/2). The ^{1}H isotope of hydrogen with only a single proton in the nucleus and half-integral spin ($I = \pm ½$) is a much used element in magnetic resonance (MR) techniques since it is the most abundant MR-active isotope in the body.

The protons in the nucleus are arranged asymmetric. A nucleus with spin is considered to rotate around an axis with a constant velocity. This rotation of an asymmetric charge induces a local magnetic field, or magnetic momentum around the nucleus parallel to the axis of rotation. Since the velocity of the rotation is considered constant, the associated magnetic momentum is also considered constant in magnitude and orientation. Just as a bar magnet the nucleus have a north and a south pole, and the axis of a nucleus with spin can

be viewed as a vector with defined orientation and magnitude. MR is based on changes made to the spin vector done by experimental manipulations. MR measurements are done on a collection of similar spins, rather than on single spins. When a collection of hydrogen atoms are unaffected by external field, protons will have spin vectors facing in every direction and thus cancel each other out, resulting into net zero spin as shown in Figure 2.

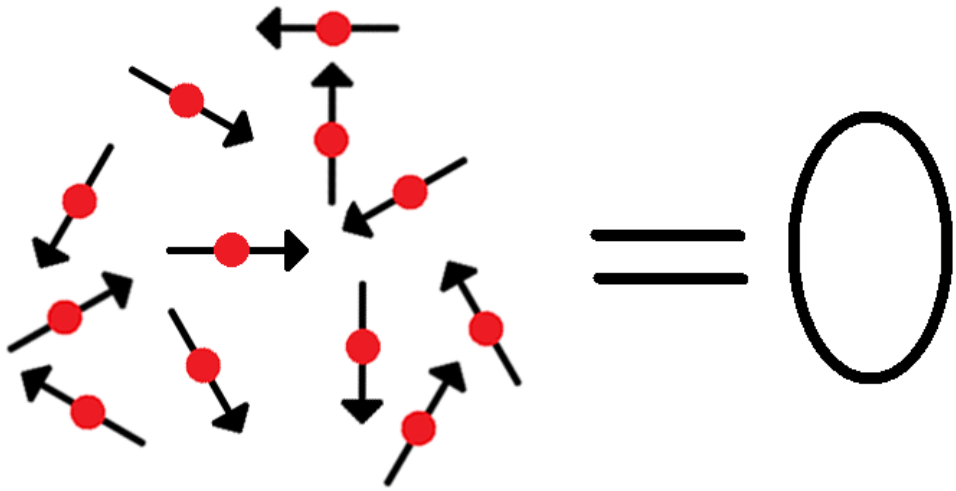

Figure 2: Net spin vector magnetization equal zero when unaffected by magnetic field.

If a collection of protons are placed in an external magnetic field, B_0, the axis of the spin vectors will align or counter-align themselves to the magnetic field, usually called z-axis, depending on their spin (½ or -½). The alignment is not stable and a an additional spin, or wobble is produced for the magnetic moment around the direction of the magnetic field, this is called precession. Imagine a gyroscope spinning around its own axis, while the top of the gyroscope also spins around in circles. The centre of that top circle is the z-axis and the direction of the magnetic field. The precession makes the magnetic moment spin around with a specific frequency. At a given magnetic field the different MR-active atoms have different precessional frequencies which are natural frequencies.

Spins with different orientation have different energy. The nuclei aligned with the magnetic field have a lower energy state (spin-up) and the counter-aligned nuclei have a higher energy state (spin-down). The number of protons in each energy state can be predicted by the Boltzmann distribution function (see Equation 2-1).

$$\frac{N_{Spin-down}}{N_{Spin-up}} = e^{-\Delta E/kT} \qquad \text{Equation 2-1}$$

where the k is Boltzmann's constant, $N_{Spin\text{-}down}$ and, $N_{Spin\text{-}up}$ are the number of protons in each energy state. ΔE is the energy difference between the energy state and T is the temperature. From equation 2-1 it is obvious that there will always be an unequal number of protons in the different energy states. This means the collection of protons will become polarized or magnetized when affected by a magnetic field. Thus, net magnetization, M_0 will be oriented in the same direction as the magnetic field and e.g. in the body the magnitude of M_0 is proportional to B_0 (see Equation 2-2)

$$M_0 = \chi B_0 \qquad \text{Equation 2-2}$$

where χ is known as the magnetic susceptibility. The arrangement is in the equilibrium when the configuration of the spins have the lowest energy. After any perturbations, such as energy absorption, the protons will naturally go back to this state. This induced magnetization, M_0, is the source of signal all in MR experiments. From Equation 2-2 one can see that both an increase of magnetic field, B_0, and magnetic susceptibility, χ, will increase the M_0, and thus increase the potential MR signal. The magnetic susceptibility describes how a substance response to an applied magnetic field. A small χ gives a diamagnetic response, which is a very weak response and for most of the materials it is the only response. Paramagnetic response is stronger than diamagnetic (larger χ) and is found in molecules with unpaired electrons. Substances with ferromagnetic response have a very large χ and are magnetically polarized even after the magnetic field is removed. A last magnetic response is super-paramagnetic. This involves particles at very small sizes (e.g.. <10 nm for Co) where the particles behave ferromagnetic when affected by a magnetic field, but paramagnetic when the magnetic field is removed [39].

2.3 Resonance

To get any information about the substance in the magnetic field their spin vector need to be moved away from the equilibrium state. This can be done by producing resonance in the nucleus. Resonance occurs when an oscillating force is applied with the natural frequency. For protons, this frequency lays in the radio frequency, RF, band for all clinical used magnetic fields. An RF pulse is used to excite the nuclei. This absorption of energy causes more hydrogen nuclei to jump from low energy spin-up to high energy spin-down. The energy difference between the two energy states corresponds to the energy required to produce resonance. As the magnetic field increases, the energy difference between the two populations increases, and a higher energy RF pulse is needed to produce resonance.

The result of the resonance is that the spin vector no longer is aligned with the magnetic field. It is pushed away from the z-axis towards the xy-plane in a cartesian system. The new angle away from the z-axis is called the flip angle. The magnitude of the flip angle depends on the amplitude and duration of the RF pulse, a normal value for the flip angle is 90°. After the spin vector is flipped 90° the spin vector spins around the z-axis with the same precessional frequency prior to the flip. If the flip angle is lower then 90° it means that fewer nuclei have been excited from low to high energy. The flip angle reflects the balance between spin-ups and spin-downs.

When resonance occurs, all the nuclei affected become coherent. This means that the spin vector is in the same position in the xyz system. When the spin vectors coherently spin in the xy-plane they will cause electromagnetic induction in a receiver coil placed around x-axis. This will produce a voltage with the same frequency as the precession frequency. The voltage is possible to measure and thus analyse.

2.4 Relaxation

When the RF pulse is turned off, the spin vector is again affected by the magnetic field, and will try to realign itself with it. To do this, the nuclei must release the energy absorbed from the RF pulse. A process were high energy nuclei release energy to become low energy and the spin vector aligns with the magnetic field is called relaxation. The magnetization along the z-axis then increases, this is called T1 recovery. T1 recovery is caused but the nucleus releasing energy to the surrounding environment, or lattice, is called spin lattice relaxation. The realising of energy causes an increase of magnetization along the z-axis. The rate of recovery is exponential as shown in Figure 3, and has a constant recovery time, T1 recovery time, for when 63% of the z-magnetization is regained. The T1 recovery time varies with surrounding substances, tissues, capability to absorb energy.

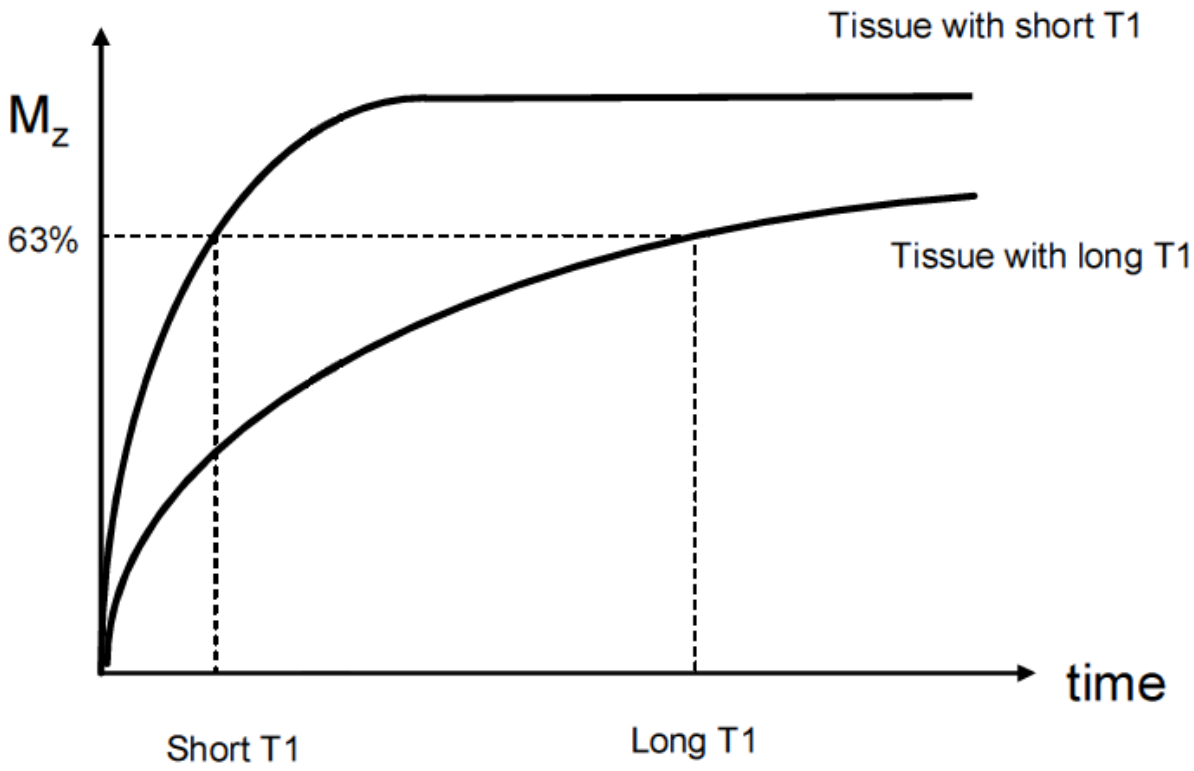

Figure 3: T1 relaxation curve for different tissue.

At the same time the magnetization in the xy-plane decreases. This is called T2 decay and is caused by loss of coherent magnetization in the xy-plane. The nuclei become incoherent, out of phase again. The rate of this decay is exponential as well with a constant T2 relaxation time for when 63% of the magnetization is lost as shown in Figure 4.

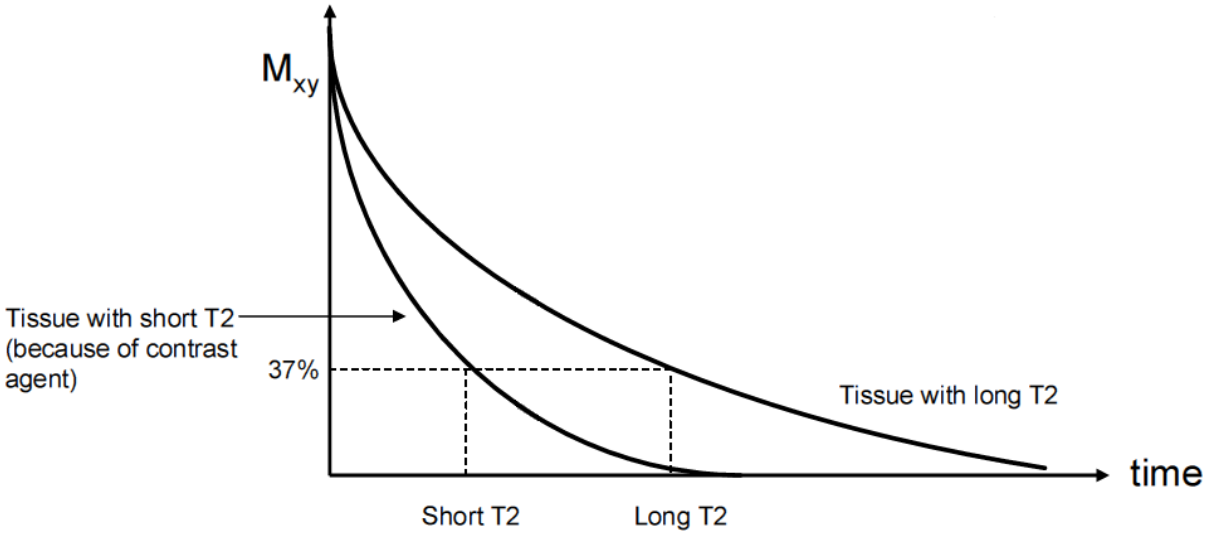

Figure 4: T2 decay curve, with example of T2 contrast-agent effect.

Different substances have different T1 relaxation- and T2 decay time resulting in different signal intensity. In T1 weighted images are based on the signal intensity of the z-magnetization, while the T2 weighted images are based on the signal intensity of the xy-magnetization. For both types of images the higher intensity is shown as bright while low intensity is dark [38, 43].

2.5 Contrast agents in MRI

Contrast agents increase the resolution in the MRI by affecting to local magnetic field and this effecting the local T1 relaxation- and T2 decay times of the tissue. When in presence of a magnetic field not only the magnetic momentum wobble, as explained earlier, but also the whole molecule spins or tumbles. When the molecule tumbles at a frequency close to the precession frequency the T1 relaxation is very efficient. Water i.e. tumbles much faster than the precession frequency, and in T1 weighted images they will appear dark. If a tumbling molecule with a large magnetic moment is in the vicinity of the fast spinning water molecule, local magnetic field fluctuations will occur. The greater the magnetic moment, the greater fluctuations. Unpaired electrons have a magnetic moment that is 500 000 times greater than that of a proton. Gadolinium with its 7 unpaired electron will thus produce large fluctuations. Gadolinium tumbles close to the precession frequency, and placed close to faster spinning molecules, such as water, it will reduce their spins. This results in decreased T1 relaxation time, and thus increased signal intensity of the water in T1 weighted images. Gadolinium is thus known as a T1 enhancement agent, other such agents include manganese and hyperpolarized helium.

The problem with Gadolinium is that pure Gd^{+3} is acute toxic, so the gadolinium need to be stabilized for it to be possible to used for clinical purposes. A method used to stabilize gadolinium is shown in Figure 5. Here the gadolinium is stabilized in a chelating complex.

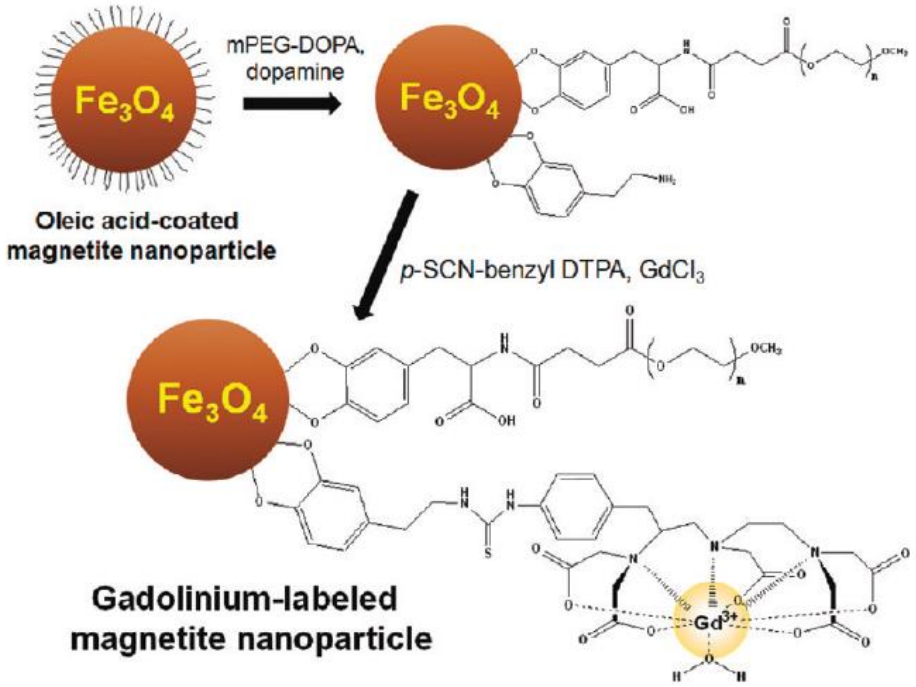

Figure 5: Two step synthesis rout to stabilize Gadolinium.

T2 decay time is also affected by large magnetic moments. The magnetic moments distorts the local magnetic field in the vicinity of the agents, causing the nearby water protons to become incoherent more rapidly. This result in significant signal loss in T2-weighted images and the nearby molecules become darker.

The effect of the contrast-agent is linear, dependent on the concentration and calculated by Equation 2-3.

$$(\frac{1}{T_i})_{Observed} = (\frac{1}{T_i})_d + r_i[C] \qquad \text{Equation 2-3}$$

Where $(1/T_i)_{Observed}$ is the values measured with the contrast agent, i = 1, 2 is equals the T1 and T2 weighted images. $(1/T_i)_d$ is the diamagnetic solvent relaxation rate without the contrast agent. The r_i is the relaxivity of the contrast agent and is measured in $mM^{-1}s^{-1}$.[44]

3. Characterization techniques

In this chapter the different techniques used in characterization of the nanoparticles will be elaborated.

3.1 Transmission electron microscopy

Transmission electron microscopy (TEM) work similar as normal light microscopy, only with electrons instead of light. The light microscopes are limited because of the wavelength of the light, electrons have much smaller wavelength and are thus able to give a higher resolution then light microscopes. With TEM it is possible to study object down to a few angstrom (10^{-10}m) in size. The TEM have an electron gun on the top of the microscope. The electrons emitted by the electron gun travel in a low vacuum through electromagnetic lenses that focus the electrons into a single beam. The electron beam scans the specimen, and depending on the density of the material, the electrons are scattered away from the beam. The electron beam then hit a fluorescent screen where the specimen will become dark spots depending on the scattering (see Figure 6). [45]

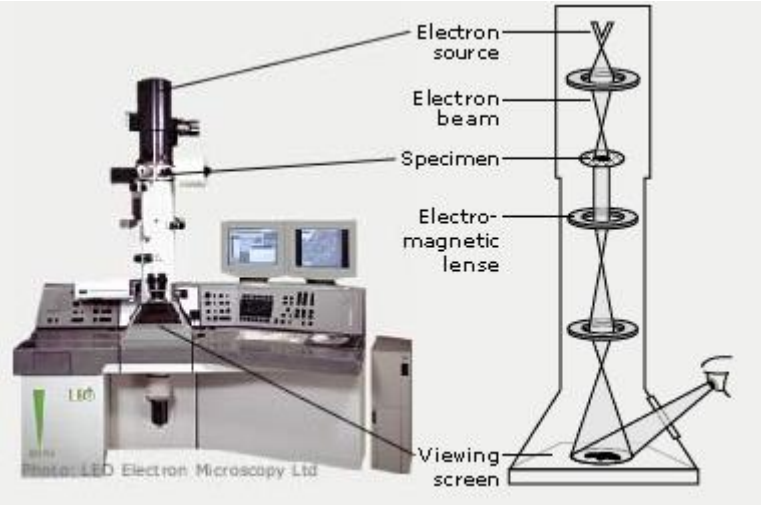

Figure 6: Illustration of TEM setup.

TEMs often have built in energy-dispersive X-ray spectroscopy (EDX). When the electron hit the specimen they excite an electron in an inner orbital, ejecting it from the orbital. An electron from an outer, higher-energy orbital jump down to an orbital to take the ejected electrons place. This electron has to release energy, which is the magnitude of the energy difference between the orbitals. This energy is released in the form of an X-ray. An energy-dispersive spectroscopy detects the number and energy of the x-rays. Because the x-ray is specific for the energy difference between the orbitals, and for the specific element the x-ray is emitted from, the EDX can determine the elemental composition of the specimen.[46]

3.2 X-ray diffraction

X-ray diffraction by crystals was discovered by Max von Laue in 1912. The wave nature of the X-rays makes it possible for scattered X-rays from a sample to interfere with each other and create intensity distribution which may be detected and shown as a X-ray diffraction pattern. This pattern is determined by the wavelength and the incident angle of the X-ray, and the atomic arrangement of the sample structure. This way it is possible to use XRD to study the crystal structure of the material. The way the waves scatter after impact, or the diffraction behaviour, is described by Braggs law (Equation 3-1).[47]

$$2d\ sin\theta = n\lambda \qquad \text{Equation 3-1}$$

Here θ is the incident angle of the X-rays, d is the spacing between the crystal planes, n is the integer and λ is the wavelength of the x-rays.

3.3 X-ray photoelectron spectroscopy

X-ray photoelectron spectroscopy (XPS) is used to analyse the surface of material. It can give the materials elemental composition, chemical state and electronic state of elements to depths of ~2 to ~10 nm from the surface. In principle the XPS work by shooting x-ray photons of specific energy at the surface in vacuum. The photons will both excite a loosely bound valence electron or a low orbital electron and eject them. The electrons ejected close to the surface of the material will travel through the vacuum and collected by detectors which use the kinetic energy (KE) to produce a spectrum of electron intensity. The kinetic energy is calculated by Equation 3-2.

$$KE = h\nu - E_{BE} - \phi_S + E_e \qquad \text{Equation 3-2}$$

Here E_e is the surface potential, ϕ_s is the work function of the sample and E_{BE} is the binding energy.[48]

3.4 Zeta potentiometer

When colloid particles are dispersed in aqueous media they bring with them a charge. The surface charge can induce ionization in the solution and form an electrical double layer of ions. Only the inner ions, the Stern layer, are strongly bound to the particle, while the other are replaced continuously. When the particle moves with Brownian motion the loosely bound outer layer will be divided in two groups. The group closer to the particle and with high enough potential, called the Slipping slope, will move around with it while the group further away will stay behind. The potential-boundary between these two groups is called the Zeta potential, see Figure 7 [49]. When an electric field is applied across and electrolyte, the charged particles will travel towards the electrode. This motion will be opposing the viscous forces acting on the particles. When these two forces are in equilibrium, the particle move with a constant velocity. This can be used to calculate the Zeta potential. The Zeta potential show how well a colloid particle can be dispersed in aqueous solutions [48].

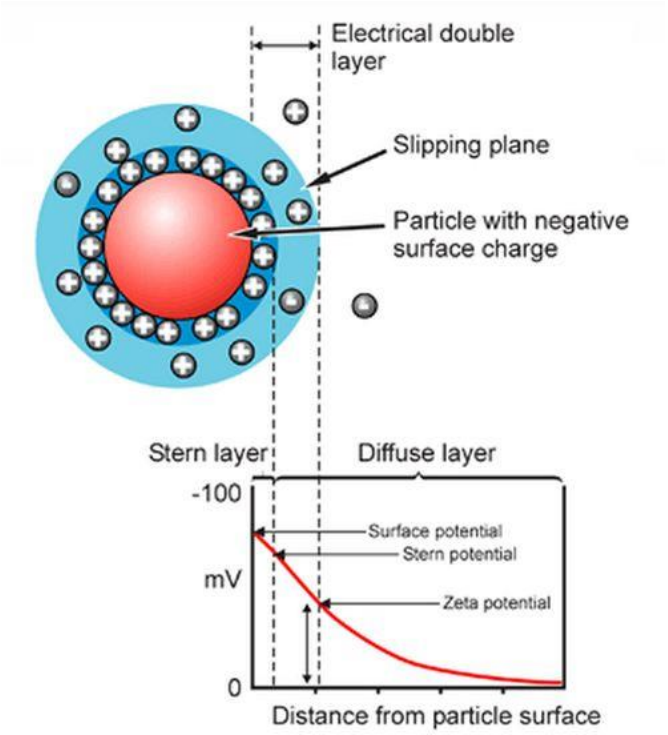

Figure 7: Schematic representation of the Zeta potential.

4. Experimental

In this chapter the experiments and analysis done in this theses will we described.

4.1 Synthesis of iron- and composite oleates.

Iron chloride ($FeCl_3.6H_2O$, 98%), cobalt chloride ($CoCl_2.6H_2O$, 98%) and gadolinium chloride ($GdCl_3.6H_2O$, 99%) were used as received from Alfa Aesar, Fluka and Sigma Aldrich respectively. All organic solvents used in this study were technical grade and purchased from VWR. Two different batches of sodium oleates were bought from J. T. Baker (batch 1) and TCI Chemicals (batch 2). For the synthesis of either pure metal oleates or composite oleates, pure $FeCl_3.6H_2O$ (20 mmol), or two different metal compunds in various amounts (20 mmol in total) were added 40 mL deionized water followed by addition of 30 mL ethanol and 70 mL hexane. The reaction mixture was stirred at 70°C for 4 hours. The organic phase was separated from the water phase and washed 4 times with deionized water to remove reaction by-product and dried with anhydrous magnesium before evaporation of hexane under vacuum at 55°C in Heidolph rotary evaporator. The molar ratio between Iron chloride and Gadolinium – and Cobalt chloride were tuned to achieve composite oleates of different composition.

4.2 Synthesis of nanoparticles

Iron oleate (1,6 g, 2,6 mmol), was mixed with various amount of surfactant, oleic acid (300 – 1200 µL, 0,96 – 3,84 mmol) and octadecene (25 mL). The reaction mixture was slowly heated up to 317°C at the rate of 2,8°C/min under vigorous stirring. The reaction time was tuned from 40-400 minuter. The temperature was strictly controlled with a PID Controller from MRClab. The reaction were done in an argon atmosphere regulated with a Schlenk line as shown in

The product was washed with hexane, butanol, and acetone. Centrifugation was used for separation of the precipitate. The dried product was dissolved in toluene for storage. The similar protocol was followed for the synthesis of composite of Gd_2O_3 nanoparticles.

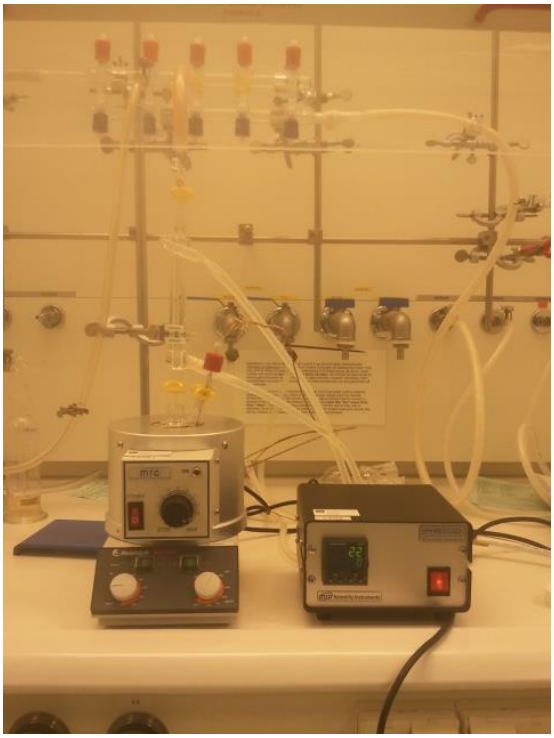

Figure 8: Reaction setup.

4.3 Phase transfer of $GdFe_2O_4$ and Gd_2O_3 nanoparticles

For the phase transfer of nanoparticles from organic aqueous, α,ω-Bis{2-[(3-carboxy-1-oxopropyl)amino]ethyl}polyethylene glycol (COOH-PEG-COOH) received from Sigma Aldrich was used. In a typical procedure, 20 mg of COOH-PEG-COOH, N-Hydroxysuccinimide (2 mg, 0,017 mmol, Sigma Aldrich), N,N'-Dicyclohexylcarbodiimide (3 mg, 0,0145 mmol, Sigma Aldrich) and 2-Hydroxytyramine hydrochloride (2 mg, 0,0105 mmol, Sigma Aldrich) were dissolved in chloroform (2 mL) and dimethylformamide (1 mL). Anhydrous sodium carbonate (10 mg) was added and the solution was stirred at room temperature for 2 hours in nitrogen atmosphere. The $GdFe_eO_4$ nanoparticles (5 mg) was dissolved in chloroform (1 mL) and added to the solution. The mixture was stirred at room temperature for 12-15 hours. The product was washed with hexane and separated by centrifuge (10 min, 10 000 rpm). The dried product was dissolved in water.

4.4 Characterization techniques

TEM images were acquired in bright-field mode using a Hitachi S-5500 electron microscope operating at 30 kV accelerating voltage. TEM grids were prepared by placing a drop (10 µL) of the nanoparticle solution on a Formvar carbon coated copper grid (Electron Microscopy Sciences) and allowing the solvent to evaporate at room temperature, prior to imaging.

The XRD analysis were done using a Bruker D8 Advance DaVinci X-ray Diffractometer with a Cu K_a radiation (λ=1,5406 Å) and a Lynxeye detector was employd for the investigation of the composite nanoparticle crystalinity, The diffraction was measured from 15° to 65° using a step size of 0,0123° and a counting time of 96 seconds per step.

XPS analyses were performed using a Kratos Axis Ultra DLD spectrometer (Kratos Analytical, UK), equipped with a monochromatizer aluminium X-ray source ($Al_{k\alpha}$, hυ = 1486.6 eV) operating at 10 mA and 13 kV (130 W). A hybrid lens (electrostatic and magnetic) mode was employed along with ad analysis area of approximately 300 µm x 700 µm. Survey spectra were collected over the range of 01200 eV binding energy with analyzer pass energy of 160 eV. XPS data were analyzed with Casa XPS software (Casa Software Ltd., UK).

Zeta potential values were measured in deionized water (pH = 6,5) using a Zetasizer Nanoseries Instrument (Malvern Instrument, UK).

Magnetic measurements were performed using a superconducting quantum interference device magnetometer (DQUID, Quantum Design MPMS-2). The samples for magnetic measurements were prepared by adding a 10-20 mg dried powder of iron oxide nanoparticles into gelatin capsules.

Fourier transformed infrared spectrometry (FTIR) was done with a Thermo Nicolet Nexus FT-IR Spectrometer, with as Smart Endurance reflection cell. Frequencies between 4000 cm^{-1} and 600 cm^{-1} were reported.

Inductively coupled plasma mass spectrometry (ICP-MS) were done with a High Resolution ICP-MS, ELEMENTS 2 from Thermo Electronics. The sample for the ICP-MS was dissolved in water and sulfuric acid.

The MRI study was done with a 7T magnet (Biospec 70/20 AS, Bruker Biospin MRI, Ettlingen, Germany) with water cooled (BGA-12, 400 mT/m) gradients. The sequences used were, for the T1-mapping, rapid acquisition with refocused echoes with variable repetition time (RARE-VTR) (TE = 8,35 ms, TRmin = 30 ms, TRmax = 20 000 ms, with 11 repetitions, NEX = 2, rare-factor = 1, total scan time = 1 houre, 27 minutes, 14 seconds and 240 ms). For the T2-mapping Multri slice multri echo (MSME) (TR = 20 000 ms, TEmin = 11 ms, number of echoes: 60, NEX = 4, total scan time = 1 hour, 25 minutes and 20 seconds).

5. Results and discussion

5.1 Synthesis of Iron Oxide

Park et al. propose an efficient approach for the synthesis of Iron oxide nanoparticles [50]. This method have been tested and developed. It was discovered that by using Iron oleate prepared from batch 1, cubic-shaped nanoparticles were observed. By analysing the iron oleate with ICP-MS small traces of calcium, 28 µg/g, and sodium, 5µg/g, were found. Other studies have used and excess amount of sodium oleates (batch 2) in synthesis of cubic-shaped nanoparticles [51]. FTIR analysis of the oleate shows a peak at 1580 cm^{-1}, as shown in Figure 9 even though calcium gives a peak at 1550 cm^{-1} the impurities may explain the shift in vibration.

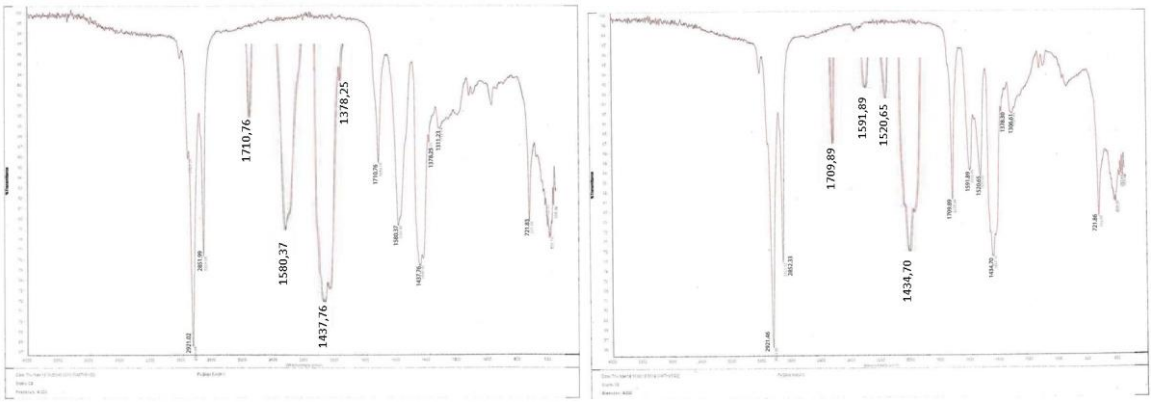

Figure 9: FTIR spectra of iron oleate from batch 1(left) and batch 2(right).

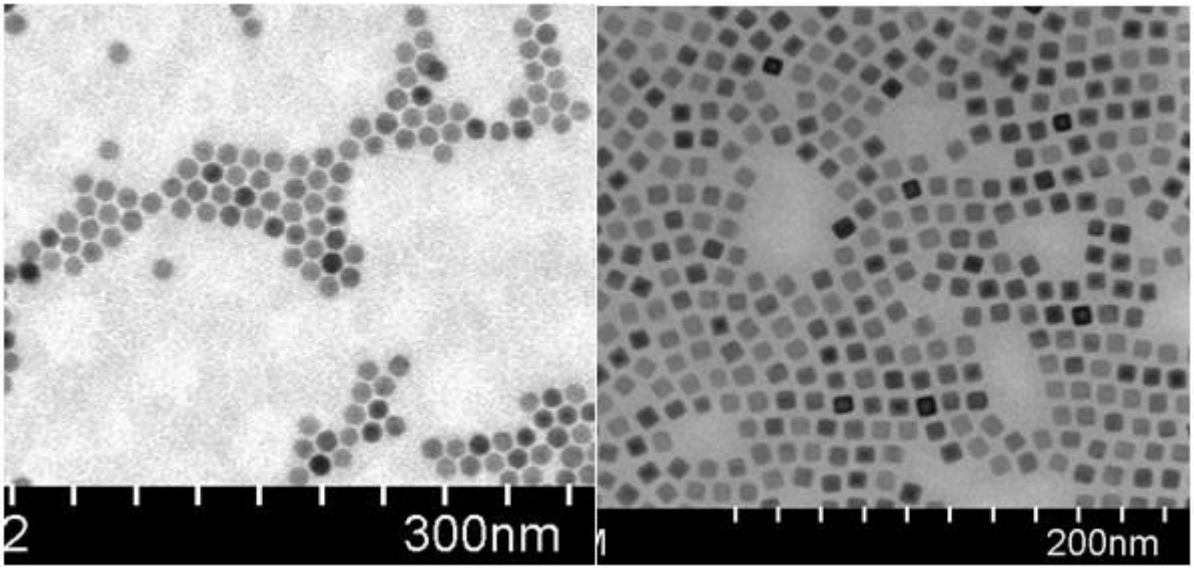

Figure 10: Iron oxide with spherical and cubic-shape.

Since the amount of calcium is much higher than that of sodium, and the FTIR analysis indicate calcium interaction to the oleate is it reasonable to believe that the calcium causes the formation of the cubic-shaped particles. Figure 10 shows example of spherical and cubic-shaped particles.

The cubic-shaped particles have very good size control and monodispersity as shown in Table 2. The particle size was affected by the amount of oleic acid, since higher amount of stabilizer can stabilize a larger surface, thus smaller particles. When synthesising larger particles, monodispersity increased with longer reaction time.

Table 2: Results from cubic-shaped iron oxide synthesis.

Reaction number	Volume oleic acid [µL]	Reaction time [minutes]	Average particle size [nm]
1	600	40	11
2	600	40	10
3	600	40	11
4	100	40	20
5	100	120	21
6	499	40	17

The magnetic properties for both the cubic and spherical iron oxide nanoparticles are summarized in Figure 11. Generally, the system is first cooled down from relatively high temperatures (here 350 K) in a zero field, zero-field cooled (ZFZ) curve is measured. The field cooled (FC) curve is usually obtained directly following the ZFZ curve upon cooling in the same applied field. All samples show super-paramagnetic behaviour above the blocking temperature (T_B) as their blocking temperature is well below that of room temperature. The T_B values for different nanoparticles are derived from the maxima of the ZFZ curves. For the cubic-shaped nanoparticles, T_B increases as nanoparticle size raises from 12 nm to 17 nm, which are coherent with literature [52]. This behaviour can be explained by Equation 5-1:

$$T_B = \frac{K_u V}{k_B \ln(\frac{\tau_m}{\tau_0})}$$ Equation 5-1

In the above expression, V is the volume of the nanoparticle, K_u is the magnetocrystalline anisotropy, k_B is the Boltzmann constant, τ_0 is the time constant characteristic of the materials (usually in the 10^{-12} – 10^{-9} s range), and τ_m is the characteristic measurement of the instrument. The anisotropic energy, $U = K_u V$, is the energy barrier between the degenerated double well potential. For the small particles, they have small volume and thus lower energy barrier and lower T_B. Interestingly, the cubic-shaped nanoparticles exhibit lower T_B than to similar size spherical nanoparticles which can be ascribed to the role played by the morphology of the nanoparticles on the effective surface anisotropy [53]. Therefore, magnetic properties also depend on the shape of nanoparticles.

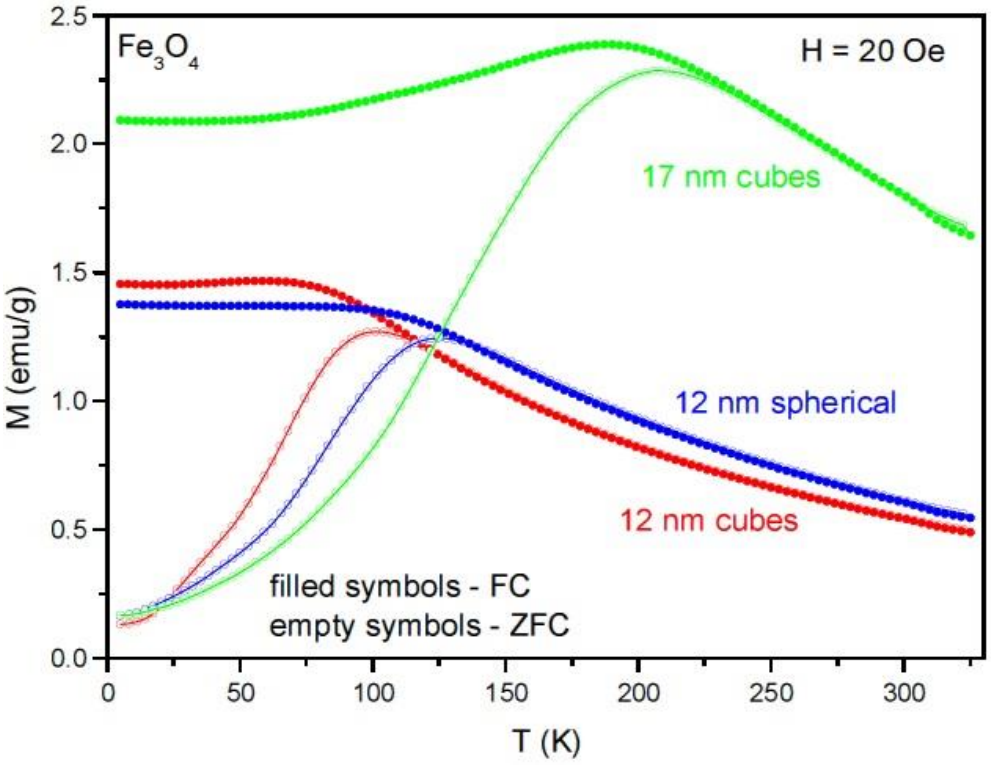

Figure 11: Temperature dependence of the ZFZ and FC magnetization of 12 and 17 nm cubes and 12 nm spherical iron oxide.

The particles were also analysed with hysterises loops (M-H) at the temperature 5 K and 300 K with the results shown in Figure 12 . All M-H curves show no remanence or coercivity – further confirming super-paramagnetic behaviour of nanoparticles [54].

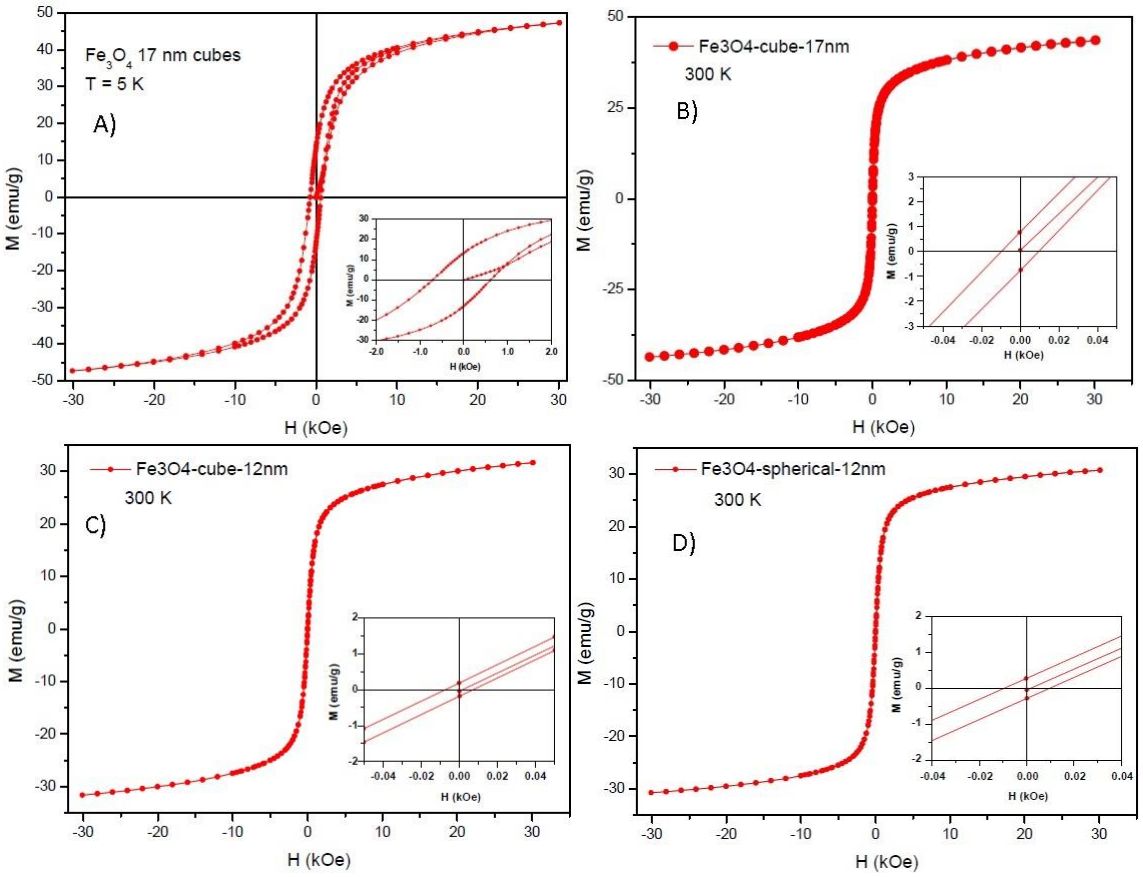

Figure 12: Hysterises loops of A) 17 nm cubes at T = 5K, B) 17 nm cubes at T = 300K, C) 12 nm cubes at T = 300K, D) 12 nm spherical at T = 300 K)

5.2 Synthesis of $Co_xFe_{3-x}O_4$ nanoparticles

With the synthesis of cubic-shaped iron oxide being well documented, the possibility to use the same synthesis method for composite cubic-shaped particles was investigated. Earlier methods of synthesising cubic-shaped composite cobalt-iron oxides have reported nanoparticles with poor control over size distribution and shape control [40]. Cobalt-Iron oleates prepared from different Fe:Co ratios were used along with different amounts of stabilizer. The particles were cubic-shaped for all the compositions, as shown in Figure 13. It is reasonable to believe that the cubic formation is the result of the same calcium impurities as for pure iron oxide.

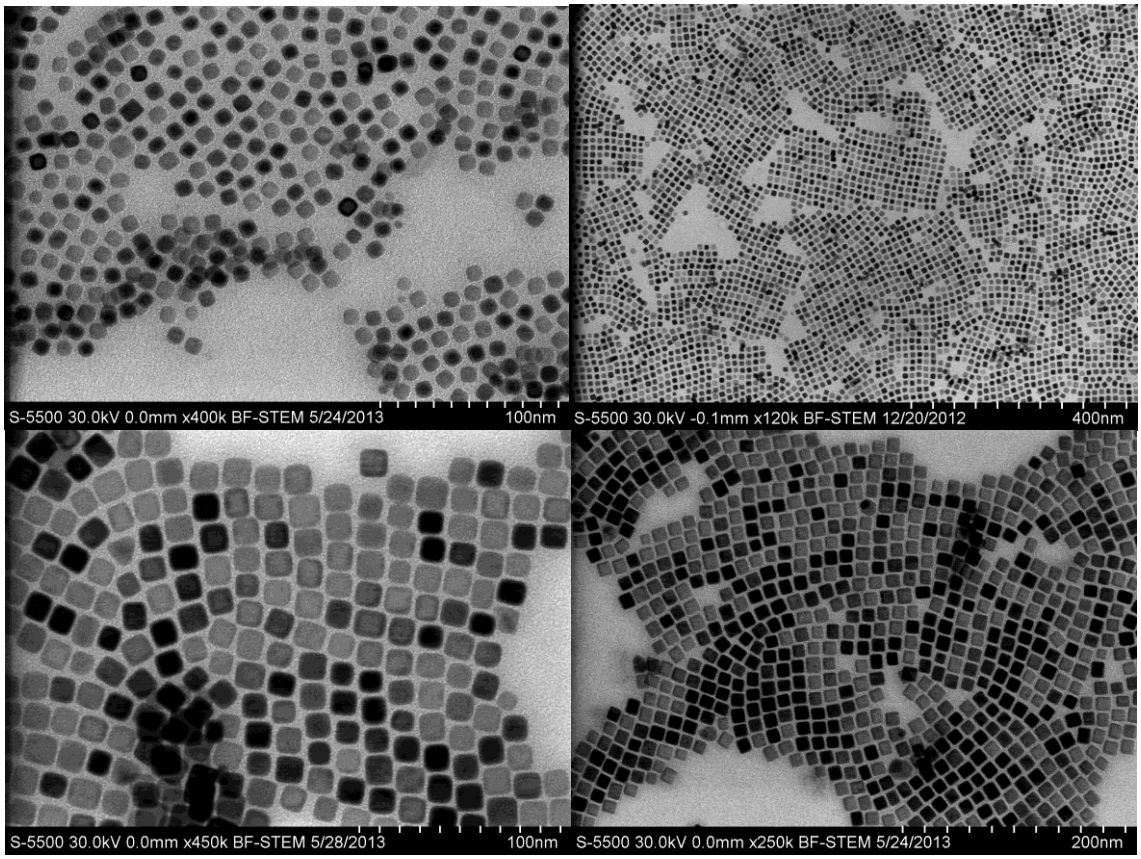

Figure 13: $Co_XFe_{3-X}O_4$ nanoparticles with the Fe:Co composition: 1:0,2 (top left), 1:0,5 (top right), 1:0,8 (lower left), 1:1 (lower right)

The results of nanoparticles synthesis from different Fe:Co ratios and amount of stabilizer are summarized in Table 3: Results of Cobalt-Iron oxide synthesis. The results show high monodispersity, and that regulating the amount of stabilizer gives good size-control.

Table 3: Results of Cobalt-Iron oxide synthesis

Sample	Iron-cobalt ratio [Fe:Co]	Oleic acid [µL]	Reaction time [minutes]	Average size [nm]	Standard size-deviation [%]
7	1:0,2	600	40	11,09	14
8	1:0,2	720	40	10,06	7
9	1:0,5	600	40	9,63	8
10	1:0,8	600	40	8,83	9
11	1:0,8	600	40	13,29	8
12	1:0,8	720	40	10,04	9
13	1:0,8	900	40	7,45	14
14	1:0,8	1200	40	4,46	13
15	1:1,0	600	40	12,31	6

Sample 9 stand out with a smaller average size than should be expected with the amount of stabilizer used. Both sample 9 and 6 shows spherical shapes, as shown in Figure 14. This shape, and the smaller size of sample 9 indicates impurities in the reaction.

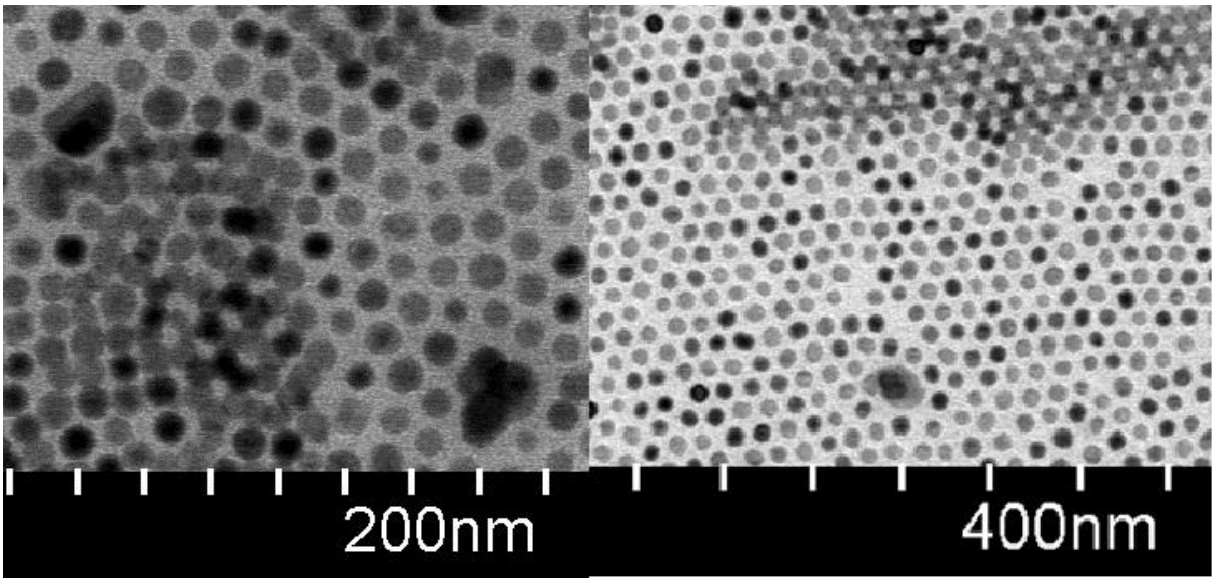

Figure 14: Sample 6 and 9 of Cobalt Iron oxide.

If one exclude sample 9 one can see a clear tendency of size control with smaller particles as more stabilizer is used. This is coherent with the results from the iron oxide synthesis. EDX analyses of the samples with different compositions were carried out to analyse the composition of the resulted particles. The results are shown in Table 4.

Table 4: Results from EDX analysis of composition of end product.

Sample	Co [atomic %]	Fe [atomic %]	Cu [atomic %]	Fe:Co
8	1,37	10,9	87,72	1:0,1
9	24,83	75,17		1:0,3
10	2,92	4,71	92,37	1:0,6

XPS study was carried out to confirm the composition of the resulted nanoparticles. The results are shown in Table 5 showing that the product have the same composition (Fe:Co) similar to the of iron and cobalt chloride added during the precursor synthesis step. These results differ slightly from the results given by the EDX analysis. This may be because the EDX is inferior analysis equipment compared to the XPS for studying material composition. Therefore, it can be concluded that the resulted nanoparticles have the same composition similar to the added metal chlorides for the precursor synthesis.

Table 5: Results from XPS study of composition of end product

Sample	Co [atomic %]	Fe [atomic %]	O [atomic %]	Si [atomic %]	Fe:Co
8	1,61	8,93	72,04	17,41	1:0,2
9	5,27	10,77	71,33	12,62	1:0,5
11	4,54	5,52	67,25	22,69	1:0,8
15	8,22	8,65	73,98	14,47	1:1

An XRD study was done of the product, as shown in Figure 15, but it was not possible to conclude with any earlier reported crystalline structure. Reason for this may be not enough sample to be analysed on the sample holder, fluorescence, cobalt giving low intensity peaks or impurities on the sample holder.

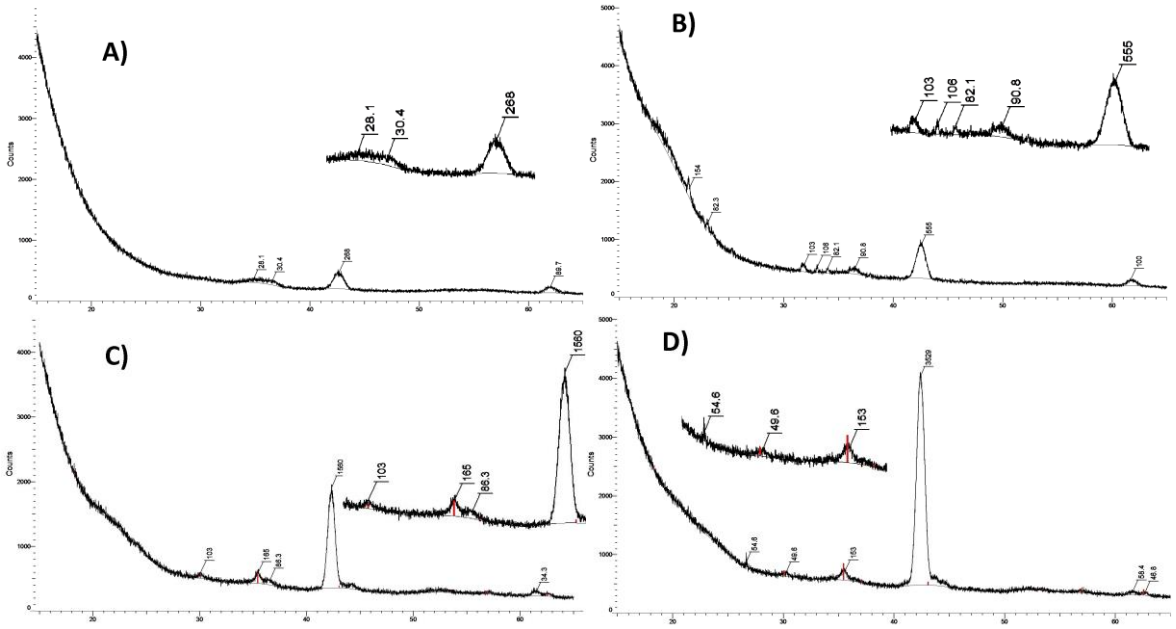

Figure 15: XRD resulst from CoXFe1-XO4 nanoparticles with the Fe:Co composition: A) 1:0,2 B) 1:0,5 C) 1:0,8 D) 1:1

Figure 16 shows cubic-shaped particles in multilayer stacking forming close packed structures similar to the tetragonal mesocrystals first reported for iron oxide by Disch et al. in 2011[55].

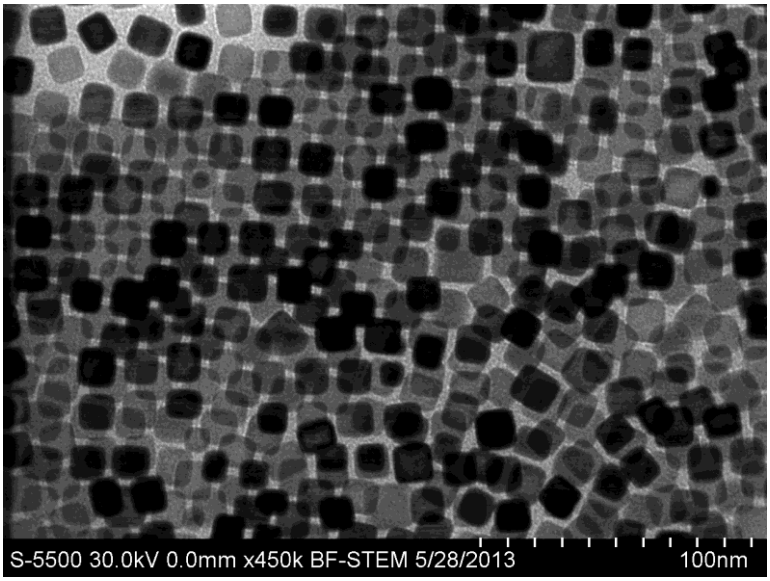

Figure 16: Cobalt iron oxide self-assembly.

5.3 Synthesis of $Gd_xFe_{3-x}O_4$ and Gd_2O_3

5.3.1 Synthesis of $Gd_xFe_{3-x}O_4$.

Gadolinium is a very useful element in MRI, but it is a significant challenge to produce gadolinium nanoparticles because of gadolinium compounds are difficult to reduce. Reactions were done to investigate if the synthesis method used for Cobalt-Iron oxide would work for Gadolinium-Iron oxide. Earlier, it was reported the synthesis of $Gd_xFe_{3-x}O_4$ via copercipitation method with a very low mole ratio (X = 0,02)[56], and gold-coated (X = 0,1)[57]. Gadolinium-Iron oleates prepared from different Fe:Gd ratios were used along with different amount of stabilizer and reaction time. The results of this are shown in table 6. The nanoparticles after the reaction needed excessive amount of cleaning to get them precipitated from the oily phase.

Table 6: Results from $Gd_xFe_{3-x}O_4$ synthesis.

Sample	Iron-cobalt ratio [Fe:Gd]	Oleic acid [µL]	Reaction time [minutes]	Average size [nm]	Standard size-deviation [%]
16	1:0,5	600	40	1,20	21
17	1:0,5	499	40	3,95	15
18	1:0,5	499	120	3,83	31
19	1:0,1	499	240	7,40	25
20	1:0,5	499	400	4,87	10

The initial stabilizer amount resulted in very small particle size as shown in Table 6 and Figure 17.

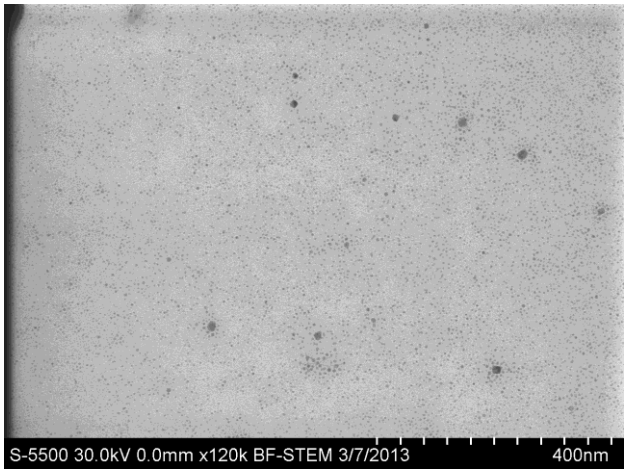

Figure 17: $Gd_xFe_{3-x}O_4$ sample with 600 µL stabilizer and 40 minute reaction time..

By prolonging the reaction time the size and quality of the nanoparticles increased as shown in Figure 18. The particles of the upper right and bottom image are very monodisperse, while the larger particles on the upper right images are of an unknown origin.

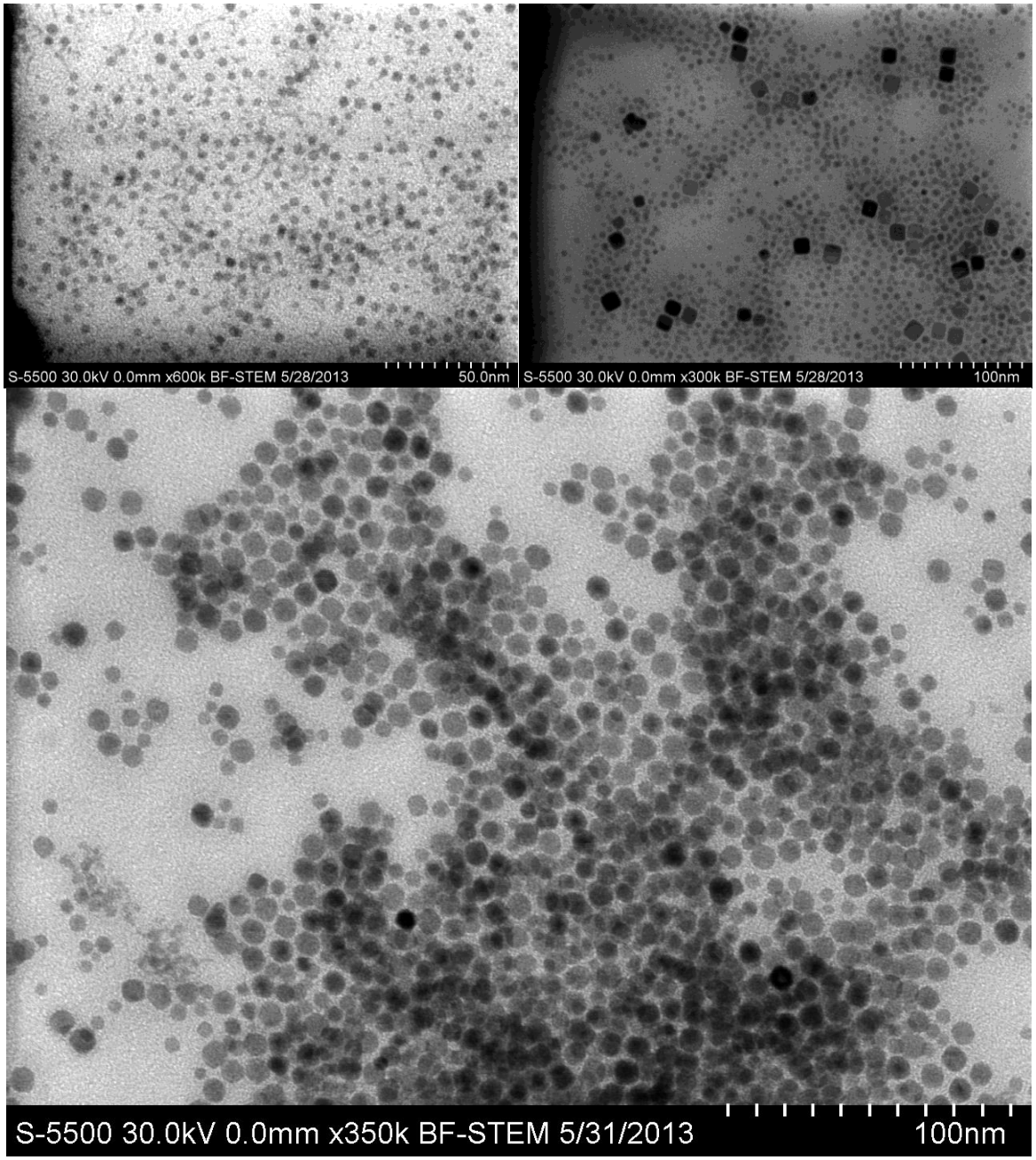

Figure 18: TEM images of $Gd_XFe_{3-X}O_4$ with 499µL stabilizer and reaction time of 40 minutes (sample 17, upper left), 120 minutes (sample 18, upper right) and 240 minutes (sample 19, bottom).

Prolonging the reaction time even further resulted in what looks like cubic-shaped particles as shown in Figure 19. It is interesting to see how different shapes the two compositions have. While nanoparticles with the Fe:Gd ratio 1:0,5 gives what seems to be cube-shaped nanoparticles, while the nanoparticles with the 1:0,1 composition gives spherical. It was not possible to find earlier reported cubic gadolinium iron oxide nanoparticles.

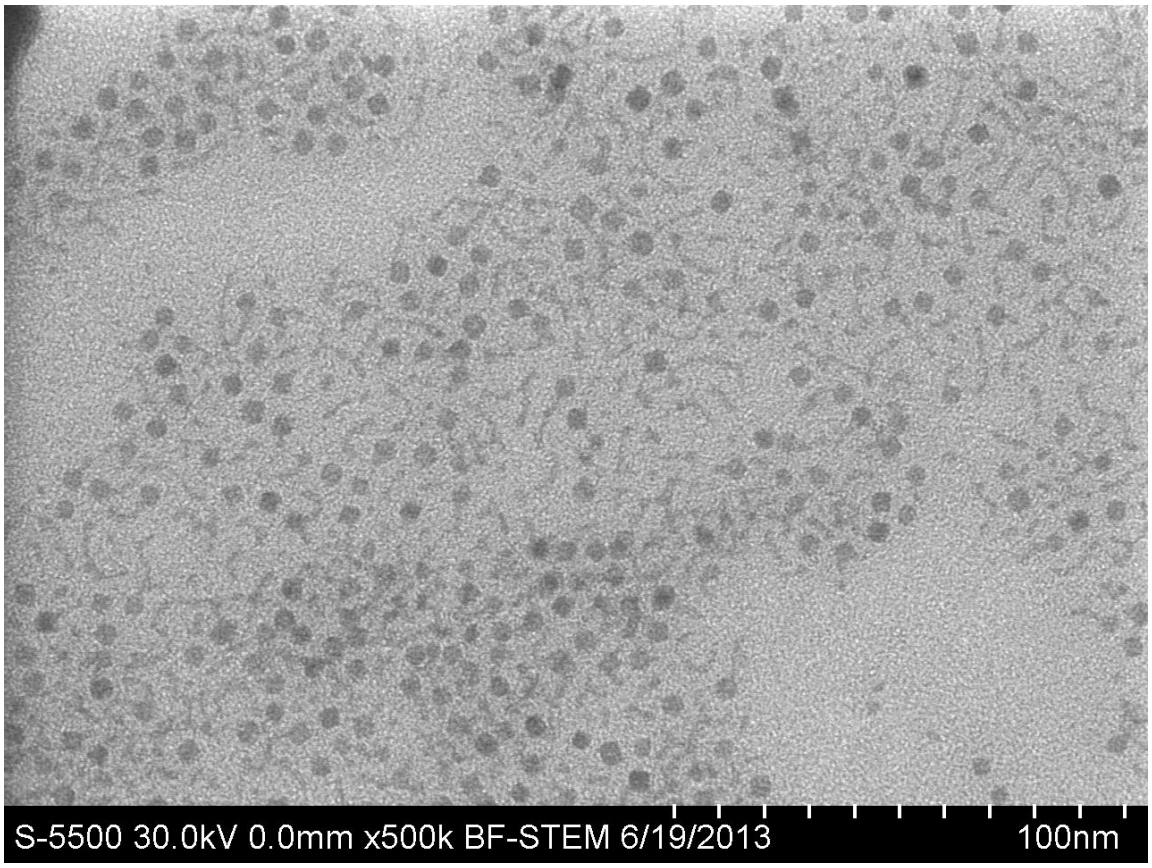

Figure 19: TEM image of $Gd_XFe_{3-X}O_4$ sample 20.

An EDX analysis was done of sample 19 clearly showing the presence of gadolinium as shown in Figure 20, even though the composition was only found to be 1:0,04.

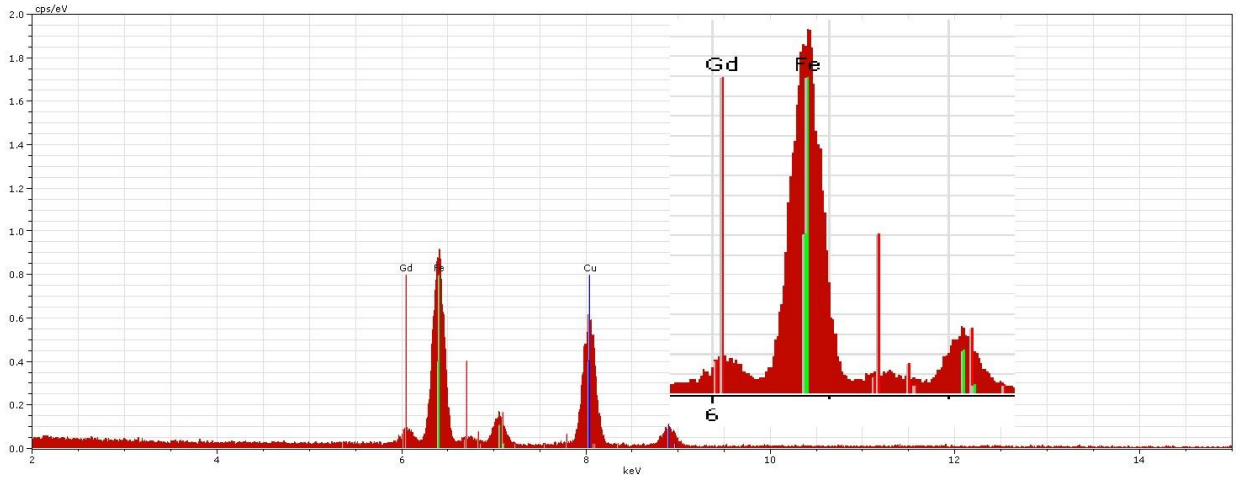

Figure 20: EDX results of sample 19.

An XPS analysis of samples from the two composition was done showing that the composition added while synthesising the precursors was intact in the product, as shown in Table 7.

Table 7: Results from XPS analysis of different composition in $Gd_XFe_{3-X}O_4$.

Sample	Gd [atomic %]	Fe [atomic %]	O [atomic %]	Si [atomic %]	Fe:Gd
17	0,29	2,93	60,67	36,11	1:0,1
19	1,45	3,02	70,80	26,09	1:0,5

5.3.2 Synthesis of Gd_2O_3.

The synthesis method has proven to be successful for synthesising $Gd_XFe_{3-X}O_4$. Thus, similar procedure was adapted for the synthesis of pure Gd_2O_3. Earlier reported methods of Gd_2O_3 synthesis are i.e. reaction between $GdCl_3$ and NaOH at elevated temperature[58, 59], and by combustion of $Gd(NO_3)_3$ and amino acid glycin[60]. Reactions with precursor made with only gadolinium was done with different amount of stabilizer and reaction time to optimize the reaction. The reaction parameters are shown in Table 8 while the results can be shown in Figure 21.

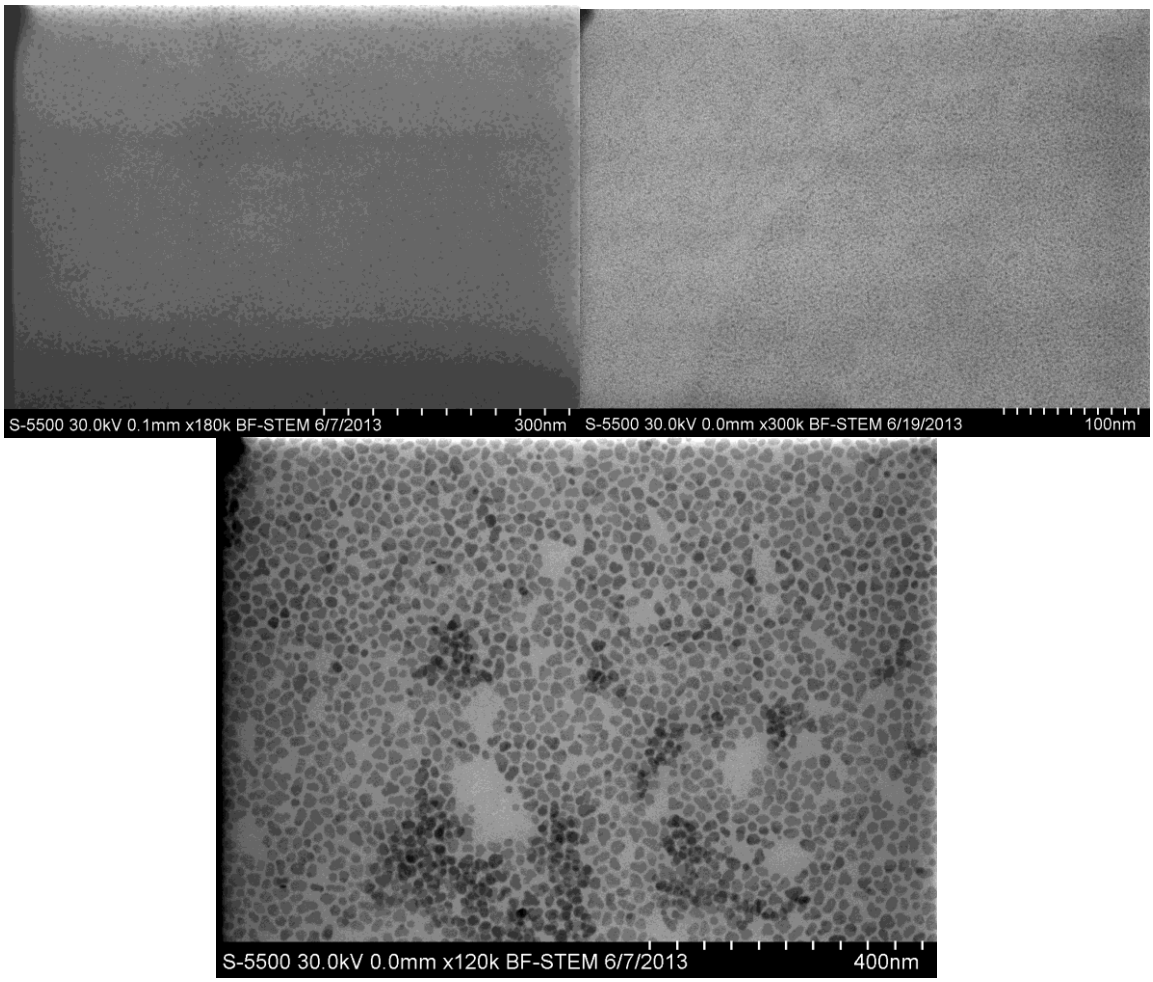

Figure 21: Sample 21(left), 22(right) and 25 (lower) from Gd_2O_3 synthesis.

Both sample 21 and 22 gave negligible product as shown in Figure 21. Increasing both the amount of stabilizer, and reaction time for sample 25 yield large polydispersed particles.

Table 8: Reaction parameters in Gd_2O_3 synthesis.

Sample	Oleic acid [µL]	Reaction time [minutes]
21	300	240
22	500	120
23	499	240
24	600	240
25	720	240

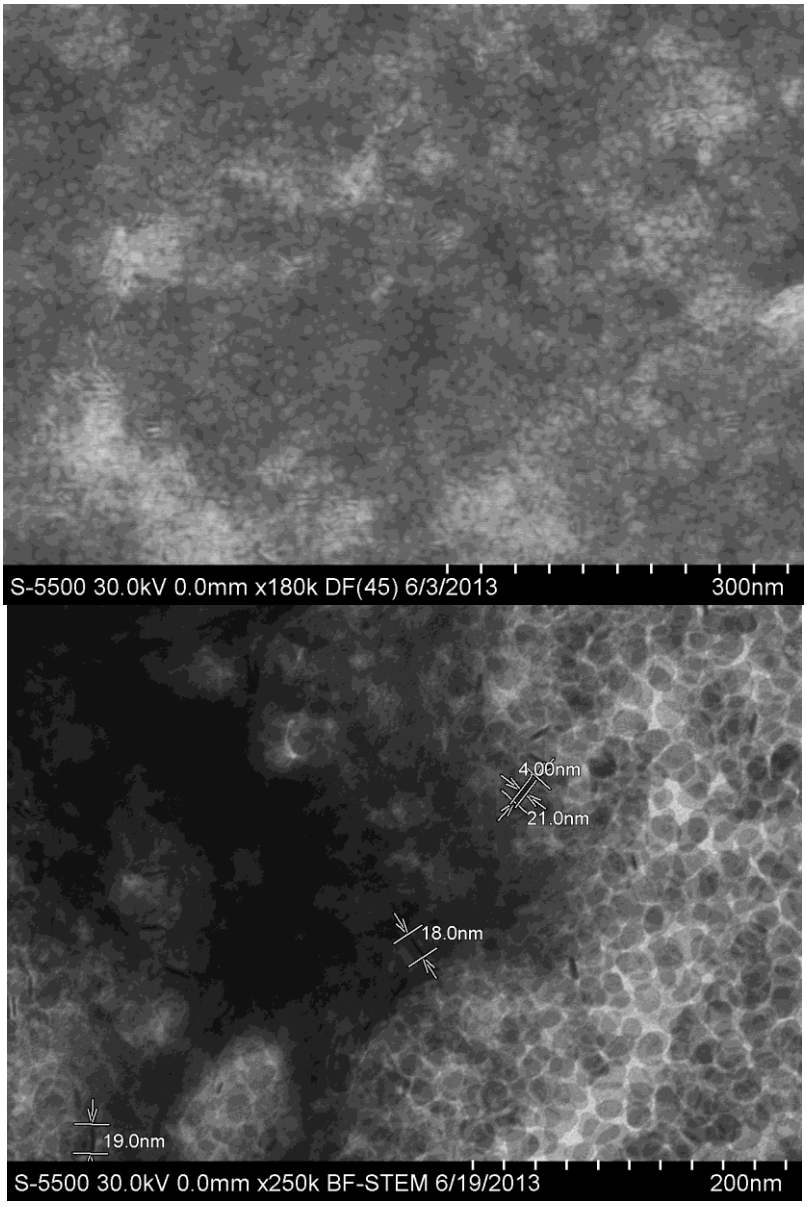

Figure 22: Sample 23 (higher) and 24 (lower) from Gd_2O_3 synthesis.

Lowering the stabilizer volume for sample 23 and 25 gave monodisperse particle as shown in Figure 22. Sample 23 are 12 nm in size and gives indication of disc-shaped nanoparticles. While sample 24 clearly shows the disc shapes. This is very interesting as it is very different from the cubic-shaped particles previously synthesized with the sodium oleates batch.

An EDX analysis was done and the results are shown in Figure 23 where the only peaks recognized are gadolinium and copper from the copper-grid.

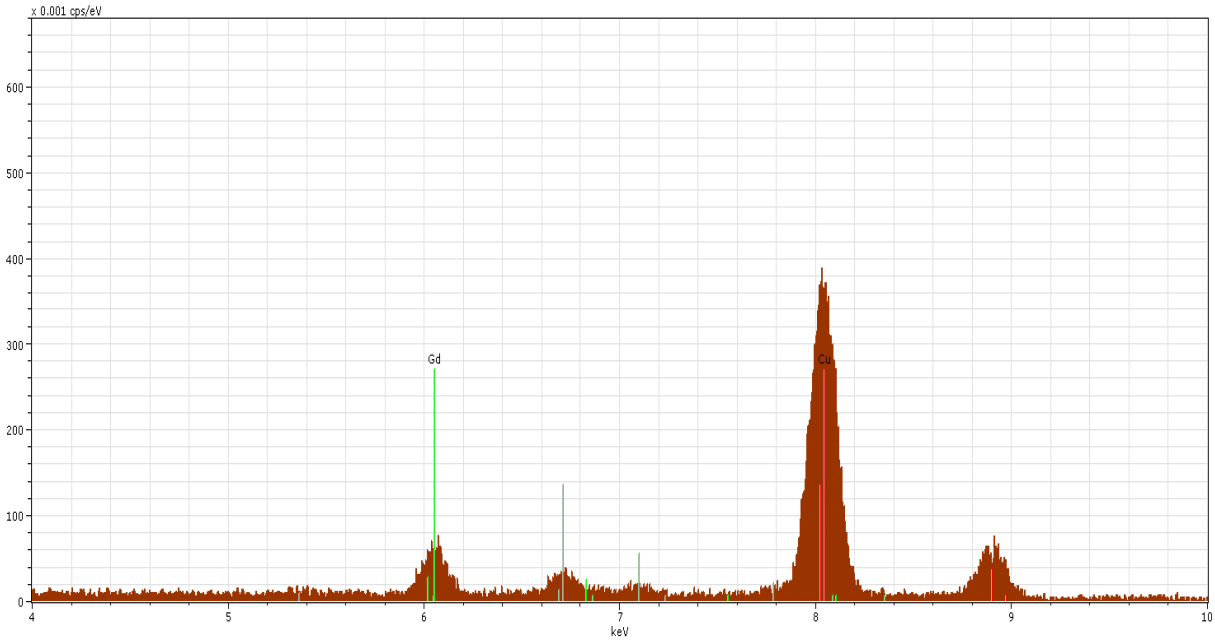

Figure 23: EDX analysis of Gd_2O_3.

Samples of different Fe:Gd composition and pure Gd_2O_3 were phase-transferred by coating them with PEG. They were then solvable in aqueous solution and their Zeta potential are shown in Table 9: Zeta potential after phase transfer..

Table 9: Zeta potential after phase transfer.

Phase-transferred sample	Zeta potential
17**	-25,18
19**	-26,36
23**	-14,6

The phase-transferred particles are shown in Figure 24. Especially sample 23** is interesting since the disc shapes are show much clearer. It is also interesting to see the discs stacking in sample 23**.

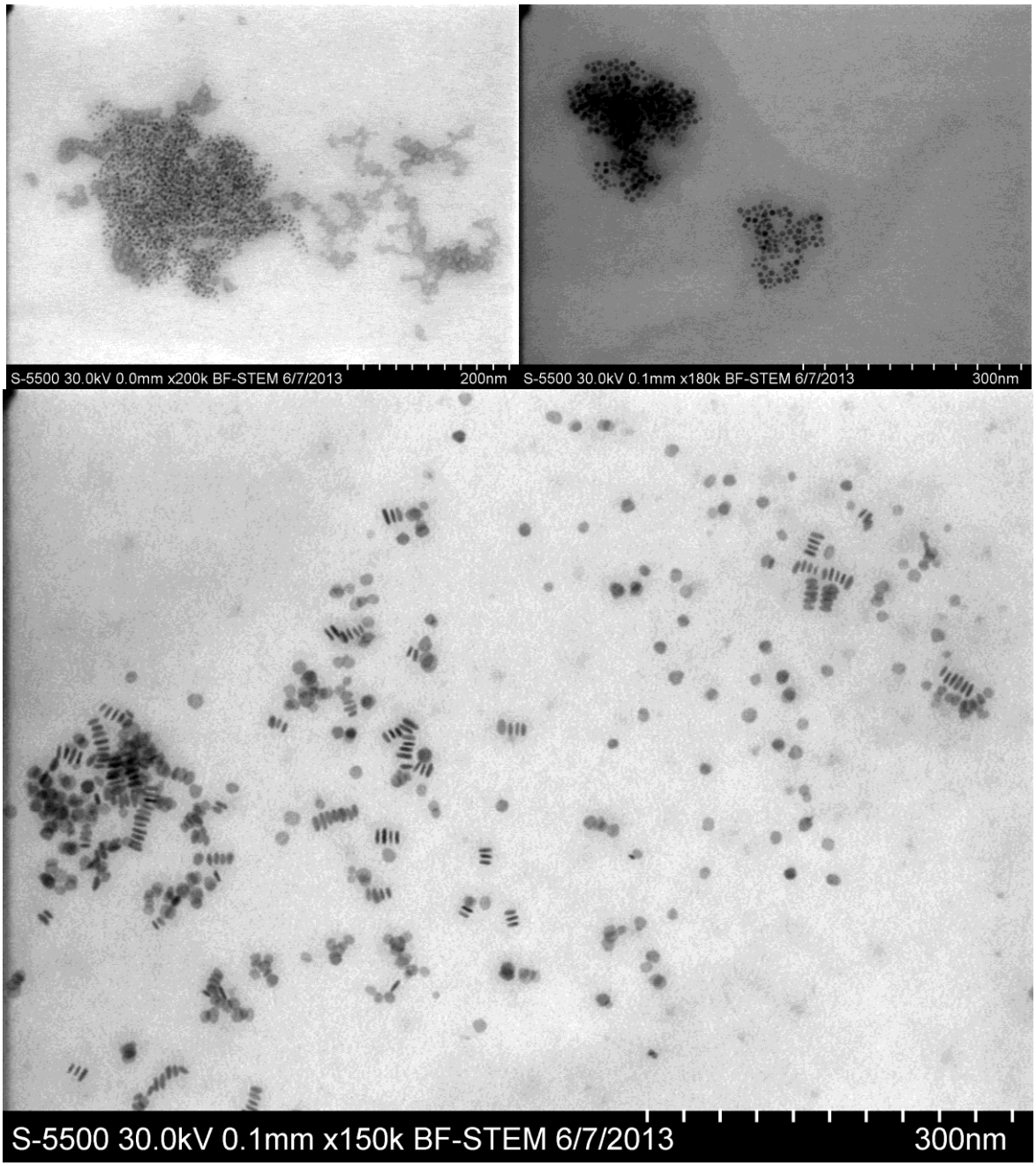

Figure 24: Sample 17(upper left), 19**(upper right) and 23** lower, after phase transfer.**

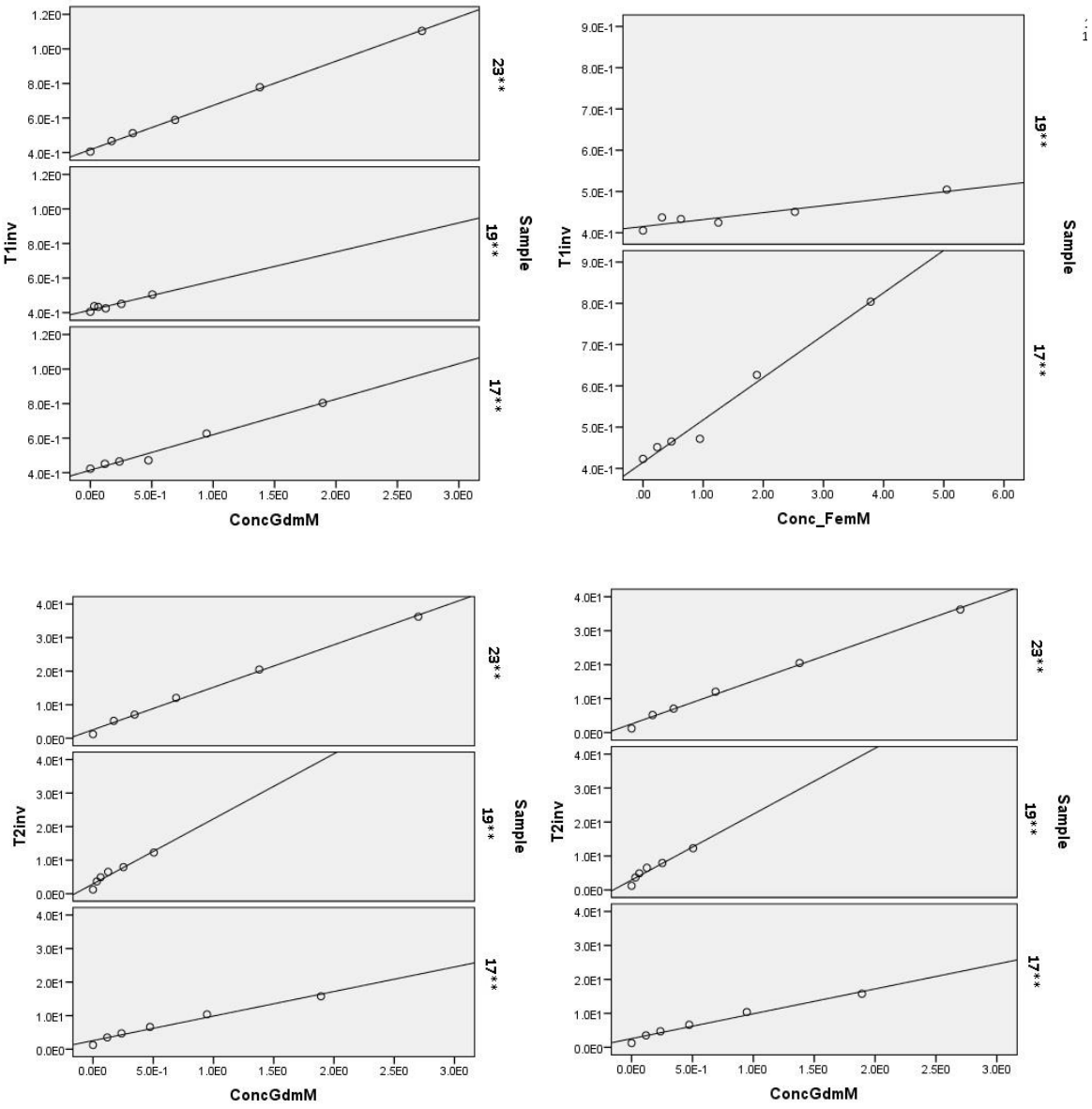

Figure 25: The different relaxation rates calculated for concentration of each element

Figure 25 shows the $1/T_i$ (i = 1, 2) observed plotted against the molar concentration of the different elements in T1-weighted and T2-weighter imaging. The relaxivity, r_i have been calculated by linear regression using equation 2-3, and the results of these calculations and the linear correlation coefficient (R^2) are shown in Table 11.

Table 10: Summery of r_1 and r_2 values.

Sample	r_1(Gd) [$mM^{-1}s^{-1}$]	R^2	r_1(Fe) [$mM^{-1}s^{-1}$]	R^2	r_2(Gd) [$mM^{-1}s^{-1}$]	R^2	r_2(Fe) [$mM^{-1}s^{-1}$]	R^2
17**	0,205	0,980	0,103	0,98	7,316	0,975	3,658	0,97
19**	0,168	0,890	0,017	0,89	19,394	0,931	1,939	0,93
23**	0,256	0,999			12,656	0,996		

Table 11 shows the total relaxivity of each sample. It clearly shows that the higher percentage gadolinium in the particle clearly gives higher relaxivity. The results also shows that the gadolinium iron oxide and the pure gadolinium oxide are able to improve surrounding water proton signal in both T1-weighted and T2-weighted images. These nanoparticles with both positive and negative contrast could be potentially utilized as molecular imaging probes.

Table 11: Total relaxivity for the particles

Sample	r_1 [$mM^{-1}s^{-1}$]	r_2 [$mM^{-1}s^{-1}$]	Ratio Fe:Gd
17**	0,21	7,475	1:0,5
19**	0,045	5,176	1:0,1
23**	0,512	25,312	Pure Gd_2O_3

6. Conclusion

A new way of synthesising cubic iron oxide nanoparticles was found by using a sodium oleate batch from J. T. Baker (batch 1). This differed from earlier results where the same method had given spherical shaped nanoparticles, when sodium oleate batch from TCI Chemicals (batch 2) was used. By analysing with FTIR and ICP-MS the differences between the two batches were found to be a higher calcium concentration in batch 1. The synthesis differs from earlier thermal decomposition methods by using a preparation step where sodium oleate was used along with metal oleate precursor. The synthesis gave cubic-shaped nanoparticles with sizes between 10 and 21 nm with high monodispersity, and regulating the amount of stabilizer used gave good size control. The nanoparticles were found to have super-paramagnetic properties above blocking.

The same synthesis protocol for cubic-shaped particles was followed where the metal oleate precursor was prepared by the addition of iron and cobalt in various proportions. The composition varied from Fe:Co = 1:0,2 to 1:1. All of the compositions gave highly monodisperse nanoparticles with sizes in the range of 4,46 nm to 13,29 nm. The particle-size was adjustable by controlling the amount of stabilizer added the solution. The atomic % of the different elements present in $Co_XFe_{3-X}O_4$ was confirmed by EDX and XPS. This method of producing cubic-shaped cobalt-iron oxide has given nanoparticles with a much higher monodispersity then previous methods. This is believed to be because of the use of composite metal precursor which gives a gentler nucleation.

The synthesis method used to make gadolinium-iron oxide. This was not as easy as cobalt iron oxide, and the reaction time had to be increase to six- to ten times that of iron oxide- and cobalt-iron oxide synthesis. The synthesis method of gadolinium-iron oxide gave nanoparticles with size ranging from 4,8 nm to 7,4 nm. Different compositions were made and it was found that with a Fe:Gd ration of 1:0,5 gave cubic-shaped particles, while composition of 1:0,1 gave spherical. The maintenance of the composite from the metal oleate in the end product was confirmed by EDX and XPS.

The same synthesis method was used to find a new method for synthesising Gd_2O_3 by thermal decomposition. The method was optimized with reaction time of 4 hours. The reaction resulting in disc-shaped particles diverged far from the cubic-shaped nanoparticles from the iron oxide-, the cobalt-iron oxide- and the gadolinium-iron oxide synthesis. Samples with both gadolinium-iron composition and pure gadolinium oxide were PEG-coated during a phase-transfer reaction. Their stability in aqueous media was tested with Zeta potential which showed the gadolinium-iron oxides had high stability, while the gadolinium oxide were less stable. Their contrast-agent abilities were tested with MRI which showed they improved proton signal of the surrounding water in both T1-weighted and T2-weighted imaging, this showing potential as contrast-agents.

7. Further work

7.1 Further work with iron oxide.

- Further mapping of the differences between the two types of oleate batches. This will be very useful to fully understand what causes the cubic-shape formation. If the differences in the compositions can be identified and quantified the shape can easily be controlled by using sodium oleate from TCI Baker and adding the right amount of chemical.
- Further investigation of size control; how large and how small particles can be made with this method by changing the amount of stabilizer and the reaction time.

7.2 Further work with cobalt iron oxide.

- Further investigate the crystalline structure of the particles with XRD analysis
- Investigate the possibility of self-assembly.

7.3 Further work with gadolinium iron oxide.

- With gadolinium iron oxide the synthesis parameters can be optimized to investigate if a better monodispersity, size and shape control can be obtained. This can be done by varying the reaction parameters such as longer reaction time.

7.4 Gadolinium oxide

- Gadolinium oxide can be investigated more in form of shape analysis of the disc shape.
- The MRI aspect of this particle should be investigated more as it may have great possibilities as a contrast-agent.

8. References

[1] W.H. Organization, Cancer mortality and morbidity, http://www.who.int/gho/ncd/mortality_morbidity/cancer/en/, 2013.

[2] K.J. Klabunde, Nanoscale Materials in Chemistry, John Wiley & Sons, Inc., New York, 2001.

[3] C.S.P. Gill, B. A.; Jones, C. W., Sulfonic acid-functionalized silica-coated magnetic nanoparticle catalysts, Journal of catalysis, 251 (2007) 145-152.

[4] D.K.L. Yi, S. S.; Ying, J. Y., Synthesis and Applications of Magnetic Nanocomposite Catalysts, Chemistry of Materials, 18 (2006) 2459-2461.

[5] A.T.B. Ngo, P.; Pileni, M. P., Spin canting and size effects in nanoparticles of nonstoichiometric cobalt ferrite, Journal of Applied Physics, 89 (2001) 3370.

[6] M.J.S. Laudenslager, R. H.; Sigmund, W. M., Electrospun materials for energy harvesting, conversion, and storage: a review., Pure and Applied Chemistry, 82 (2010).

[7] B.X. Koo, H.; Slater, M. D.; Prakapenka, V. B.; Balasubramanian, M.; Podsiadlo, P.; Johnson, C. S.; Rajh, T.; Schevchenko, E., Hollow Iron Oxide Nanoparticles for Application in Lithium Ion

Batteries, Nano Letters, 12 (2012) 2429-2435.

[8] K.L. Woo, H. J.; Ahn, J.; Park, Y. S., Sol-Gel Mediated Synthesis of Fe_2O_3 Nanorods, Advanced Materials, 15 (2003) 1761-1764.

[9] W.G. Zhao, J.; Zhang, L.; Chen, H.; Shi, J. , Fabrication of Uniform Magnetic Nanocomposite Spheres with a Magnetic Core/Mesoporous Silica Shell Structure, Journal of American Chemical Society, 127 (2005) 8916-8917.

[10] R.R. Yuhong, J. G.; He, L.; Kulkarni, H.; Lee, D. K.; Messersmith, P. B., Facile, high efficiency immobilization of lipase enzyme on magnetic iron oxide nanoparticles via a biomimetic coating, BMC Biotechnology, 11 (2011).

[11] C.M. Xu, L.; Roes, I.; Miranda-Nieves, D.; Nahrendorf, M.; Ankrum, J. A.; Zhao, W.; Karp, J. M., Nanoparticle-based monitoring of cell therapy, Nanotechnology, 22 (2011).

[12] Ø.P. Olsvik, T.; Skjerven, Ø.; Cudjoe, K. S.; Hornes, E.; Ugelstad, J.; Uhlén, M., Magnetic Separation Techniques in Diagnostic Microbiology, Clinical Microbiology Reviews, 7 (1994) 43-54.

[13] A.K.C. Gupta, A. S. G., Lactoferrin and ceruloplasmin derivatized superparamagnetic ion oxide nanoparticles for targeting cell surface receptors, Biomaterials, 25 (2003) 3029-3040.

[14] R.Y. Qiao, C.; Gao, M., Superparamagnetic iron oxide nanoparticles: from preparations to in vivo MRI applications, Journal of Materials Chemistry, 19 (2009) 6274-6293.

[15] F.L. Loe, S.; Fattahi, H.; Elst, L. V.; Muller, R. N., Superparamagnetic nanosystems based on iron oxide nanoparticles for biomedical imaging, Nanomedicine, 6 (2011) 519-528.

[16] Q.Q.C. Pankhurst, J.; Jones, S. K.; Dobson, J., Applications of magnetic nanoparticles in biomedicine, Journal of Physics D: Applied Physics, 36 (2003) R167-R181.

[17] C.C.C. Berry, A. S. G., Functionalisation of magnetic nanoparticles for applications in biomedicine, Journal of Physics D: Applied Physics, 36 (2003) R198-R206.

[18] H.B.S. Na, I. C.; Hyeon, T., Inorganic Nanoparticles for MRI Contrast Agents, Advanced Materials, 21 (2009) 2133-2148.

[19] J.S. Lai, K. V. P. M.; Ulman, A.; Loss, K.; Yang, N.; Cui, M.; Vogt, T.; Estournès, C.; Lock, D. C., Mixed Iron-Manganese Oxide Nanoparticles, The journal of physical chemistry. B, 108 (2004) 14876-14883.

[20] C.L.C. Warner, W.; Mackie, K. E.; Neiner, D.; Saraf, L. V.; Droubay, T. C.; Warner, M. G.; Addleman, R. S., Manganese Doping of Magnetic Iron Oxide Nanoparticles: Tailoring Surface Reactivity for a Regenerable Heavy Metal Sorbent, Langmuir, 28 (2012) 3931-3937.

[21] D.G. Nandi, K.; Gosh, A. K.; De, A.; Banerjee, S.; Gosh, U. C., Manganese-incorporated iron(III) oxide-graphene magnetic nanocomposite: synthesis, characterization, and application for the arsenic(III)-sorption from aqueous solution, Journal of Nanoparticle Research, 14 (2012).

[22] M.A. Bellusci, C.; Fiorani, D.; La Barbera, A.; Padella, F.; Peddis, D.; Pilloni, M.; Secci, D., Manganese iron oxide superparamagnetic powder by mechanochemical processing. Nanoparticles functionalization and dispersion in a nanofluid, Journal of Nanoparticle Research, 14 (2012).

[23] Y.K. Li, E.; Borg, S.; Schüler, D., The Periplasmic Nitrate Reductase Nap Is Required for Anaerobic Growth and Involved in Redox Control of Magnetite Biomineralization in *Magnetospirillum gryphiswaldense*, Journal of Bacteriology, 194 (2012) 4847-4856.

[24] Z.L. Liu, T.; Ehling, J.; Fokong, S.; Bornemann, J.; Kiessling, F.; Gätjens, J., Iron oxide nanoparticle-containing microbubble composites as contrast agents for MR and ultrasound dual-modality imaging, Biomaterials, 32 (2011) 6155-6163.

[25] H.G.M. El-Shobaky, M. M., Effect of Li_2O and CoO-doping of CuO/Fe_2O_3 system on its surface and catalytic properties, Applied Surface Science, 253 (2007) 9407-9413.

[26] H.J. Cui, Y.; Ren, W.; Wang, W., Facile and ultra large svale synthesis of nearly monodispersed $CoFe_2O_4$ nanoparticles by a low temperature sol-gel route, Journal of Sol-Gel Science and Technology, 55 (2010) 36-40.

[27] M.S. Starowicz, P.; Zukrowski, J.; Przewoznik, J.; Lemanski, A.; Kapusta, C.; Banas, J., Electrochemical synthesis of magnetic iron oxide nanoparticles with controlled size, Journal of Nanoparticle Research, 13 (2011) 7167-7176.

[28] M.M.P. Islam, L. V.; Jeong, J.; Kim, C., A facile route to sonochemical synthesis of magnetic iron oxide (Fe_3O_4) nanoparticles, Thin Solid Films, 519 (2011) 8277-8279.

[29] C.X. Cheng, F.; Gu, H., Facile synthesis and morphology evolution of magnetic iron oxide nanoparticles in different polyol processes, New Journal of Chemistry, 35 (2011) 1072-1079.

[30] D.T. Li, W. Y.; Selomulya, C.; Woodward, R. C.; Amal, R.; Rosche, B., Flame-Sprayed Superparamagnetic Bare and Silica-Coated Maghemite Nanoparticles: Synthesis, Characterization, and Protein Adsorption-Desorption, Chemistry of Materials, 18 (2006) 6403-6413.

[31] A.H.S. Lu, E. L.; Schüth, F, Magnetic Nanoparticles: Synthesis, Protection, Functianolization, and Application., Anggewandte Chemie International Edition, 46 (2007) 1222-1244.

[32] S.G.H. Kwon, T., Formation Mechanisms of Uniform Nanocrystals via Hot-Injection and Heat-Up Methods, small, (2011) 1-8.

[33] L.C. Carbone, P. D., Colloid heterostructured nanocrystals: Synthesis and growth mechanism, Nano Today, 5 (2010) 449-493.

[34] M.V.B. Kovalenko, M. I.; Lechner, R. T.; Hesser, G.; Schäffler, F.; Heiss, W., Fatty Acid Salts as Stabilizers in Size- and Shape-Controlled Nanocrystal Synthesis: The Case of Inverse Spinel Iron Oxide, Journal of the American Chemical Society, 129 (2007) 6352-6353.

[35] Y.X. Xia, Y.; Lim, B.; Skrabala, S. E., Shape-Controlled Synthesis of Metal Nanocrystals: Simple Chemistry Meets Complex Physics?, Nanostructures, 48 (2009) 60-103.

[36] C.H.T. Ho, C. P.; Chung, C. C.; Tsai, C. Y.; Chen, F. R.; Lin, H. J.; Lai, C. H., Shape-Controlled Growth and Shape-Dependent Cation Site Occupancy of Monodisperse Fe_3O_4 Nanoparticles, Chemistry of Materials, (2011).

[37] C.W. Yang, J.; Hou, Y., Fe_3O_4 nanostructures: synthesis, growth mechanism, properties and applications, Chemical Communications, 47 (2011) 5130-5141.

[38] C.R. Westbrook, C. K.; Talbot, J., MRI in practice, 4. ed., Wiley-Blackweel, 2011.

[39] N.S. Bao, L.; Wang, Y. A.; Ma, J.; Mazumdar, D.; Gupta, A. , Controlled Growth of Monodisperse Self-supported Superparamagnetic Nanostructures of Spherical and Rod-like CoFe2O4 Nanocrystals, Journal of American Chemical Society, 131 (2009) 12900-12901.

[40] N.S. Bao, L.; Wang, Y.; Padhan, P.; Gupta, A., A Facile Thermolysis Route to Monodisperse Ferrite Nanocrystals, Journal of the American Chemical Society, 129 (2007) 12374-12375.

[41] S.R. Mohapatra, S. R.; Panda, A. B., One-port synthesis of uniform and spherically assembled functionalized MFe_2O_4 (M = Co, Mn, Ni) nanoparticles, Colloids and Surfaces A: Physicochemichal and Engineering Aspects, 384 (2011) 453-460.

[42] G.F. Aylward, T., SI Chemical Data, 5 ed., John Wiley & Sons Australia., Milton, 2002.

[43] M.A.S. Brown, R. C., MRI: Basic principles and applications, 4. ed., Wiley-Blackwell, Hoboken, New Jersey, 20102.

[44] E.M. PhD Huuse, Contrast agents in MRI, in: D.o.c.a.m.i. NTNU (Ed.), 2012.

[45] Nobelprize.org, The Transmission Electron Microscope, http://www.nobelprize.org/educational/physics/microscopes/tem/index.html, 2013.

[46] J.I. Goldstein, Scanning electron microscopy and X-ray microanalysis, 3 ed., Kluwer Academic/Plenum Publishers, New York, 2003.

[47] T.E. Jenkins, Semiconductor science: growth and characterization techniques, Prentice Hall, New York, 1995.

[48] R.J. Hunter, Zeta potential in colloid science: principles and applications, Academic Press, London, 1981.

[49] Malvern, Zeta potential measurement using laser Doppler electrophoresis (LDE), http://www.malvern.com/labeng/technology/zeta_potential/zeta_potential_lde.htm, 2013.

[50] J.A. Park, K.; Hwang, Y.; Park, J. G.; Noh, H. J.; Kim, J. Y.; Park, J. H.; Hwang, N. M.; Hyeon, T., Ultra-lagre-scale syntheses of monodisperse nanocrystals, Nature Materials, 3 (2004) 891-895.

[51] A.L.-M.L.M. Shavel, Shape control of iron oxide nanoparticles, Physical Chemistry Chemical Physics, 11 (2009) 3762-3766.

[52] C.R.C. Lin, R. K.; Wang, J. S.; Sung, T. W., Magnetic properties of monidisperse iron oxide nanoparticles, Journal of Applied Physics, 99 (2006) 08N710.

[53] G.S. Salazar-Alvarez, J. Q. V.; Bergmann, I.; Vasilakaki, M.; Trohidou, K. N.; Ardisson, J. D.; Macedo, W. A. A.; Mikhaylova, M.; Muhammed, M.; Baró, M. D.; Nogués, J., Cubic versus Spherical Magnetic Nanoparticles: The Role of Surface Anistropy, Journal of American Chemical Society, 130 (2008) 13234-13239.

[54] S.A. Tanwar, T. P. S.; Singh, S. P.; Pasricha, R., Magnetic Field Dependence of Blocking Temperature in Oleic Acid Functionalized Iron Oxide Nanoparticles, Journal of Superconductivity and Novel Magnetism, 25 (2012) 2041-2045.

[55] S.W. Disc, E.; Hermann, R. P.; Salazar-Alvarez, G.; Busch, P.; Brückel, T.; Bergström, L.; Kamali, S. , Shape Induced Symmetry in Self-Assembled Mesocrystals of Iron Oxide Nanocubes, Nano Letters, 11 (2011) 1651-1656.

[56] P.C. Drake, H. J.; Shih, P. S.; Kao, C. H.; Lee, K. F.; Kuo, C. H.; Lin, X. Z.; Lin, Y. J., Gd-doped iron-oxide nanoparticles for tumor therapy *via* magnetic field hyperthermia, Journal of Materials Chemistry, 17 (2007) 4914-4918.

[57] D.E.C. Gheorghe, L.; Karmonik, C.; Brazdeikis, A.; Penaloza, J. M.; Young, J. K.; Drezek, R. A.; Bikram, M., Gold-silver alloy nanoshell: a new candidate for nanotherapeutics and diagnostics, Nanoscale Research Letters, 6 (2011) 12.

[58] R.F. Bazzi, M. A.; Louis, C.; Lebbou, K.; Zhang, W.; Dujardin, C.; Roux, S.; Mercier, B.; Ledoux, G.; Bernstein, E.; Perriat, P.; Tillement, O., Synthesis and properties of europium-based phosphors on the nanometer scale: Eu_2O_3, Gd_2O_3:Eu, and Y_2O_3:Eu, Journal of Colloid and Interface sience, 273 (2004) 191-197.

[59] F.P. Söderlind, H.; Petoral Jr., R. M.; Käll, P. O.; Uvdal, K., Synthesis and characterisation of Gd_2O_3 nanocrystals functionalised by organic acids., Journal of Colloid and Interface sience, 288 (2006) 140-148.

[60] J.Y. Miyawaki, M.; Imai, H.; Yorimitsu, H.; Isobe, H.; Nakamura, E.; Iijima, S., Synthesis of Ultrafine Gd2O3 Nanoparticles Inside Single-Wall Carbon Nanohorns, The journal of physical chemistry. B. Letters, 110 (2006) 5179-5181.

Appendix

A. Results from ICP-MS analysis

Resultater ikke beregnet tilbake til fast materiale

Date of analyses: 23.11.12 sekvens 58

Counting digits = 3

Isotope	Na23(MR)		Ca43(MR)	
Parameteres	Conc.		Conc.	
Sample ID	µg/L	RSD, %	µg/L	RSD, %
Start statistical calculations				
Henrik-Fe-26-7mg-47ml	3	6,3	16	1,3

Resultater beregnet tilbake til fast materiale , 26.7 ml materiale ble løst i 47 ml

syre, slutkons 0.6M HNO3. Først stod det ca 1 time i ultralydbad v 80 C med 50% v/v HNO3, deretter ble det fortynnet til 47 ml med yyyterligere en tine i ultralydbad, var ikke synlig partikler da, men lettere blakket løsning.

Date of analyses: 23.11.12 sekvens 58

Counting digits = 3

Isotope	Na23(MR)		Ca43(MR)	
Parameteres	Conc.		Conc.	
Sample ID	µg/g	RSD, %	µg/g	RSD, %
Start statistical calculations				
Henrik-Fe-26-7mg-47ml	5	6,3	28	1,3

Merknader til resultatene:

Usikkerheten i målingen anngis med Rsd, se ark idl-25%-fig., flesteparten av elementene er < deteksjonsgrense, høy rsd. Fe er det 2.8 %, forventet max 7% ut fra formlene. Urenheter - det ble ikke tatt med en blank, derfor har jeg ikke kontroll på om noen av urenhetene kan komme fra røret, syra skal være av ultra ren grad, dette var bare et forsøk på å løse opp stoffet, vi bør nok ta en repitisjon for å verifisere disse resultaene, vi kan lage en mere konsentrert løsning, og dermd få sikrere tall på ureinhetene.

B. EDX spectre of $Co_XFe_{3-X}O_4$

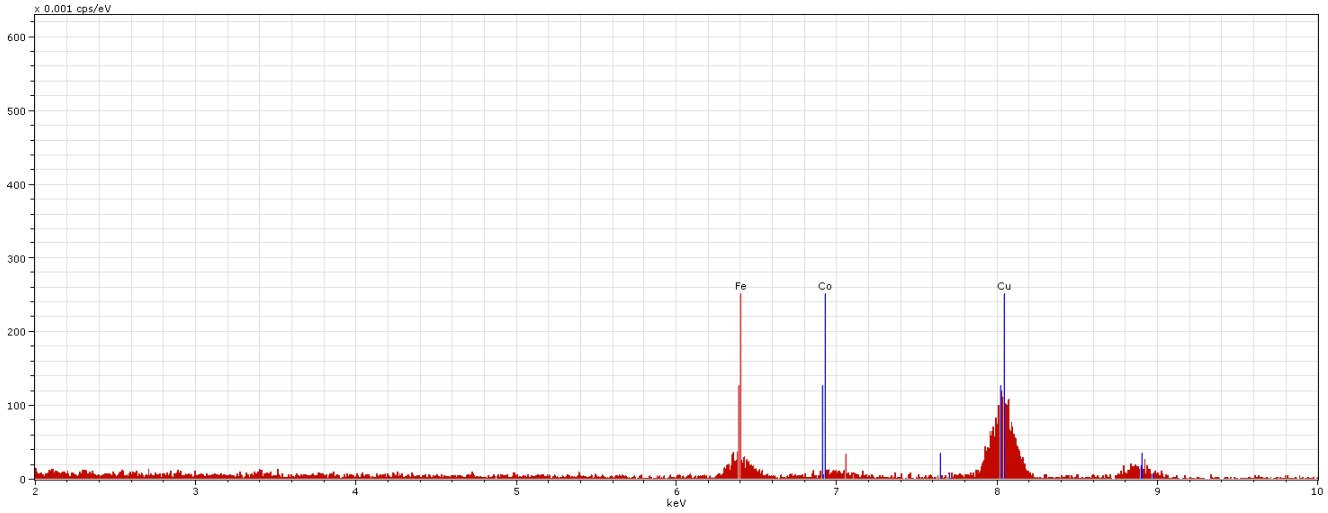

Figure B-26: EDX spectre of sample 8.

Bruker Nano GmbH, Germany 5/24/2013

Quantax

Results HW-11-1-001.spx
Date: 5/24/2013

Element	series	[wt.%]	[norm. wt.%]	[norm. at.%]	[wt.%]	[norm. wt.%]	Error in wt.% (3 Sigma)
Iron	K-series	2,72581078	4,709922956	5,312575735	2,7258	4,709922956	0,60176
Copper	K-series	53,45600959	92,36653129	91,56248872	53,456	92,36653129	4,986047
Cobalt	K-series	1,691966645	2,923545757	3,124935545	1,692	2,923545757	0,482565
	Sum:	57,87378702	100	100			

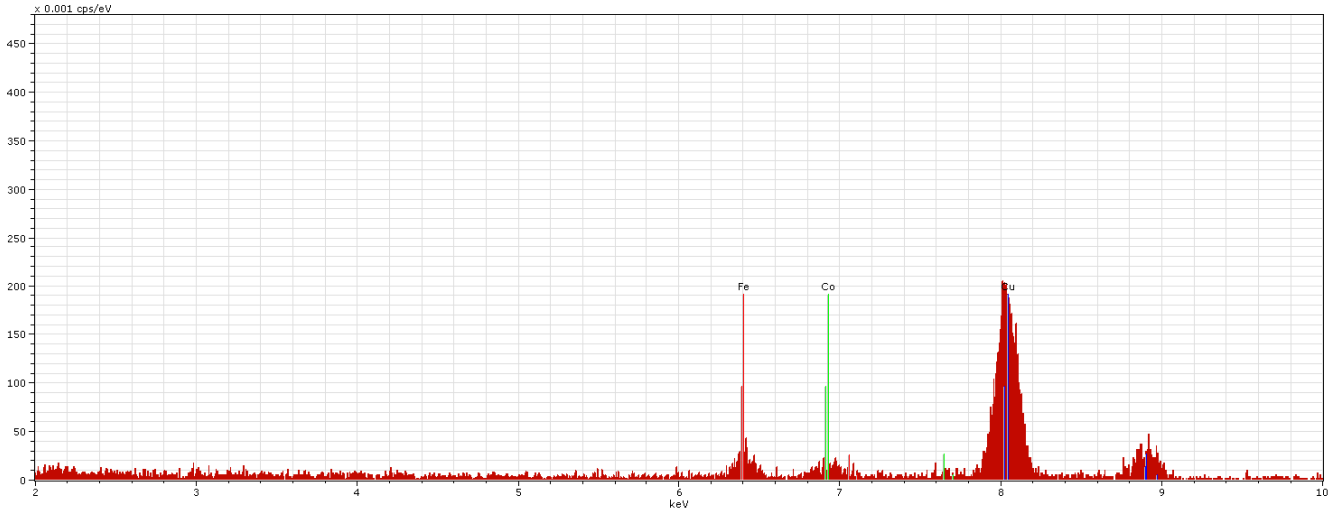

Figure B-27: EDX spectre of sample 10.

Bruker Nano GmbH, Germany		5/24/2013
	Quantax	
Results	HW-14-1-001.spx	
Date:	5/24/2013	

Element	series	[wt.%]	[norm. wt.%]	[norm. at.%]	[wt.%]	[norm. wt.%]	Error in wt.% (3 Sigma)
Iron	K-series	4,210367075	10,90334195	12,20980022	4,210367	10,90334	0,743293
Copper	K-series	33,87427114	87,72222354	86,33167843	33,87427	87,72222	3,426774
Cobalt	K-series	0,530743126	1,374434506	1,458521353	0,530743	1,374435	0,285196
	Sum:	38,61538134	100	100			

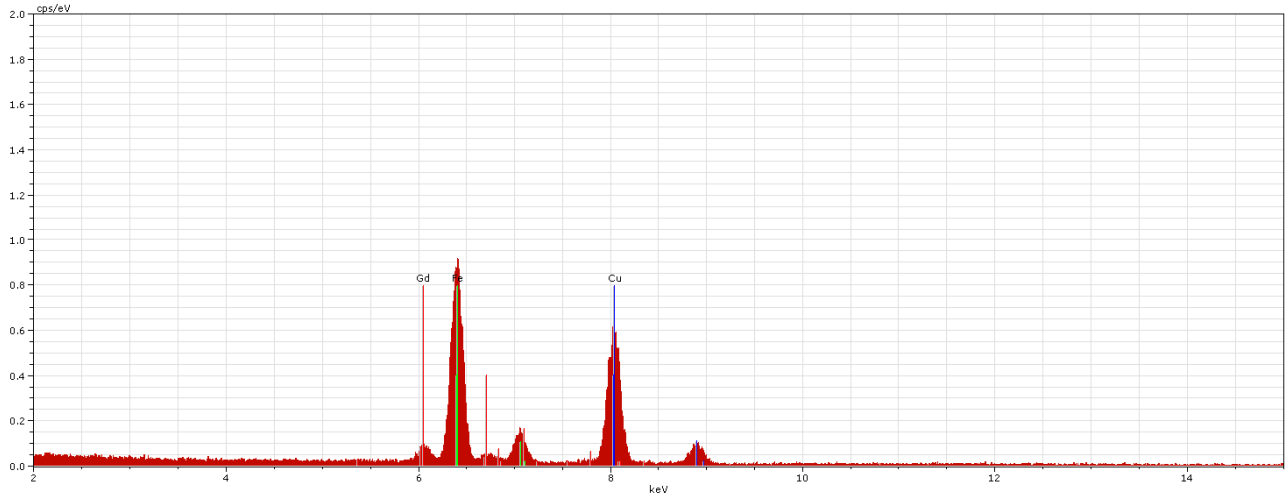

Figure B-28: EDX spectre of sample 19.

Bruker Nano GmbH, Germany		5/31/2013
	Quantax	
Results	HWS-20-001.spx	
Date:	5/31/2013	

Element	series	[wt.%]	[norm. wt.%]	[norm. at.%]	[wt.%]	[norm. wt.%]	Error in wt.% (3 Sigma)
Gadolinium	L-series	3,592248	5,293511	2,090939	3,592248	5,293511	0,434332
Iron	K-series	26,87759	39,60663	44,05104	26,87759	39,60663	2,180323
Copper	K-series	37,3915	55,09986	53,85802	37,3915	55,09986	2,95469
	Sum:	67,86134	100	100			

C. Calculation of relaxivity.

Table C-a: Appendix r1 and r2 values.

Sample	r_1(Gd) [$mM^{-1}s^{-1}$]	R^2	r_1(Fe) [$mM^{-1}s^{-1}$]	R^2	r_2(Gd) [$mM^{-1}s^{-1}$]	R^2	r_2(Fe) [$mM^{-1}s^{-1}$]	R^2
17**	0,205	0,980	0,103	0,980	7,316	0,975	3,658	0,975
19**	0,168	0,890	0,017	0,890	19,394	0,931	1,939	0,931
23**	0,256	0,999			12,656	0,996		

Table C-b: Calculation of elemental concentration in sample tubes

Sample numer		**23****		**19****		**13****	
Molweight g/mol		362,5		259,204545		332,95	
Start concentrastion [g/L] and [mol/L]		0,5 Fe	0,00137931 Gd	0,48 Fe	0,00185182 Gd	0,63 Fe	0,00189218 Gd
Tube nr: mol/l	**1**	0	0,00275862	0,00505042	0,00050504	0,00378435	0,00189218
	2	0	0,00137931	0,00252521	0,00025252	0,00189218	0,00094609
	3	0	0,00068966	0,0012626	0,00012626	0,00094609	0,00047304
	4	0	0,00034483	0,0006313	6,313E-05	0,00047304	0,00023652
	5	0	0,00017241	0,00031565	3,1565E-05	0,00023652	0,00011826

Table C-c: Calculation of T1 and T2 in sample tubes for sample 23**

Tube nr	T1inv [s^{-1}]	T2inv [s^{-1}]	c Gd2O3 [mmol/L]
1	0,7062069	34,9131034	1,37931034
2	0,35310345	17,4565517	0,68965517
3	0,17655172	8,72827586	0,34482759
4	0,08827586	4,36413793	0,17241379
5	0,04413793	2,18206897	0,0862069

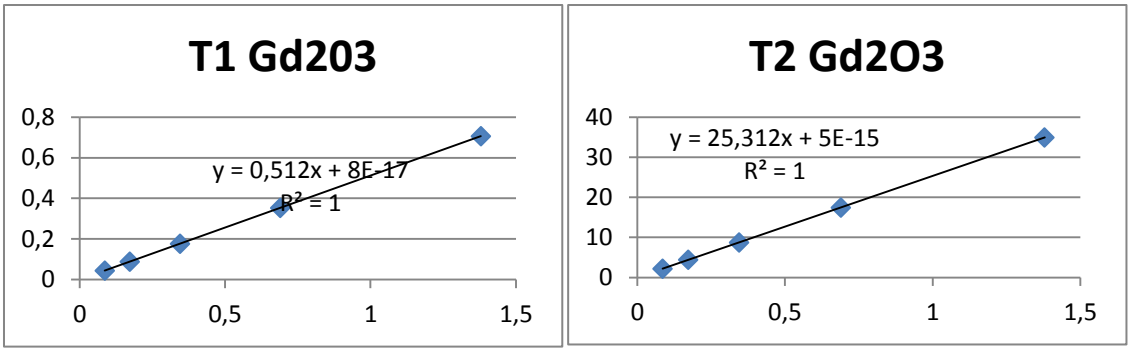

Figure C-29: T1 and T2 vs. mmol/L for sample 23''

Table C-d: Calculation of T1 and T2 in sample tubes for sample 19**

Tube nr	T1invGd [s^{-1}]	T1invFe [s^{-1}]	Snitt T1 inv [s^{-1}]	T2invGd [s^{-1}]	T2invFe [s^{-1}]	Snitt T2 inv [s^{-1}]	c 19** [mmol/L]
1	0,084847	0,085857	**0,085352**	9,794777	9,792757	**9,793767**	1,892176
2	0,042423	0,042928	**0,042676**	4,897388	4,896378	**4,896883**	0,946088
3	0,021211	0,021464	**0,021338**	2,448694	2,448189	**2,448441**	0,473044
4	0,010605	0,010732	**0,010669**	1,224347	1,224094	**1,224220**	0,236522
5	0,005302	0,005366	**0,005334**	0,612173	0,612047	**0,612110**	0,118261

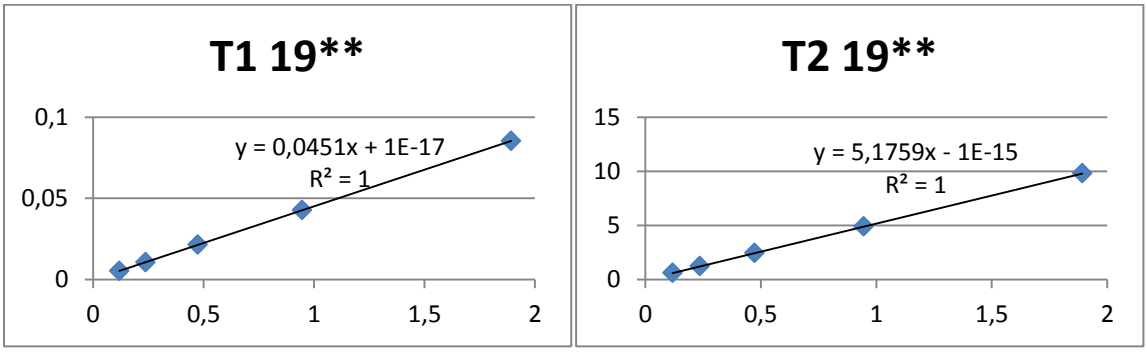

Figure C-30: T1 and T2 vs. mmol/L for sample 19''

Table C-e: Calculation of T1 and T2 in sample tubes for sample 17**

Tube nr	T1invGd [s^{-1}]	T1invFe [s^{-1}]	Snitt T1 inv [s^{-1}]	T2invGd [s^{-1}]	T2invFe [s^{-1}]	Snitt T2 inv [s^{-1}]	c 17** [mmol/L]
1	0,387896	0,389788	**0,388842**	13,843160	13,843160	**13,843160**	1,851819
2	0,193948	0,194894	**0,194421**	6,921580	6,921580	**6,921580**	0,925910
3	0,096974	0,097447	**0,097211**	3,460790	3,460790	**3,460790**	0,462955
4	0,048487	0,048724	**0,048605**	1,730395	1,730395	**1,730395**	0,231477
5	0,024244	0,024362	**0,024303**	0,865197	0,865197	**0,865197**	0,115739

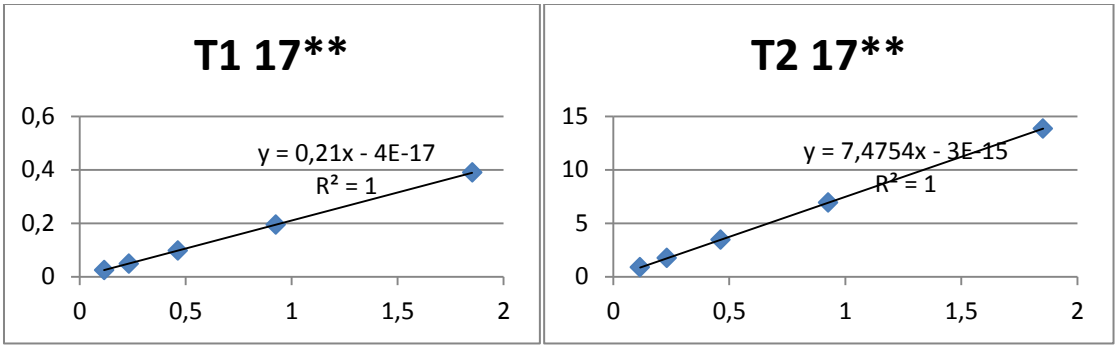

Figure C-31: T1 and T2 vs. mmol/L for sample 17''